



# CHORUS

This is the accepted manuscript made available via CHORUS. The article has been published as:

## Particle rearrangement and softening contributions to the nonlinear mechanical response of glasses

Meng Fan, Kai Zhang, Jan Schroers, Mark D. Shattuck, and Corey S. O'Hern

Phys. Rev. E **96**, 032602 — Published 6 September 2017

DOI: [10.1103/PhysRevE.96.032602](https://doi.org/10.1103/PhysRevE.96.032602)

# Particle rearrangement and softening contributions to the nonlinear mechanical response of glasses

Meng Fan,<sup>1,2</sup> Kai Zhang,<sup>3</sup> Jan Schroers,<sup>1,2</sup> Mark D. Shattuck,<sup>4,1</sup> and Corey S. O'Hern<sup>1,2,5,6</sup>

<sup>1</sup>*Department of Mechanical Engineering and Materials Science,  
Yale University, New Haven, Connecticut, 06520, USA*

<sup>2</sup>*Center for Research on Interface Structures and Phenomena,  
Yale University, New Haven, Connecticut, 06520, USA*

<sup>3</sup>*Department of Chemical Engineering, Columbia University, New York, New York 10027, USA*

<sup>4</sup>*Department of Physics and Benjamin Levich Institute,  
The City College of the City University of New York, New York, New York, 10031, USA*

<sup>5</sup>*Department of Physics, Yale University, New Haven, Connecticut, 06520, USA*

<sup>6</sup>*Department of Applied Physics, Yale University, New Haven, Connecticut, 06520, USA*

(Dated: August 22, 2017)

Amorphous materials such as metallic, polymeric, and colloidal glasses, exhibit complex preparation-dependent mechanical response to applied shear. In particular, glassy solids yield, with a mechanical response that transitions from elastic to plastic, with increasing shear strain. We perform numerical simulations to investigate the mechanical response of binary Lennard-Jones glasses undergoing athermal, quasistatic pure shear as a function of the cooling rate  $R$  used to prepare them. The ensemble-averaged stress versus strain curve  $\langle\sigma(\gamma)\rangle$  resembles the spatial average in the large size limit, which appears smooth and displays a putative elastic regime at small strains, a yielding-related peak in stress at intermediate strain, and a plastic flow regime at large strains. In contrast, for each glass configuration in the ensemble, the stress-strain curve  $\sigma(\gamma)$  consists of many short nearly linear segments that are punctuated by particle-rearrangement-induced rapid stress drops. To explain the nonlinearity of  $\langle\sigma(\gamma)\rangle$ , we quantify the shape of the small stress-strain segments and the frequency and size of the stress drops in each glass configuration. We decompose the stress loss (*i.e.*, the deviation in the slope of  $\langle\sigma(\gamma)\rangle$  from that at  $\langle\sigma(0)\rangle$ ) into the loss from particle rearrangements and the loss from softening (*i.e.*, the reduction of the slopes of the linear segments in  $\sigma(\gamma)$ ), and then compare the two contributions as a function of  $R$  and  $\gamma$ . For the current studies, the rearrangement-induced stress loss is larger than the softening-induced stress loss, however, softening stress losses increase with decreasing cooling rate. We also characterize the structure of the potential energy landscape along the strain direction for glasses prepared with different  $R$ , and observe a dramatic change of the properties of the landscape near the yielding transition. We then show that the rearrangement-induced energy loss per strain can serve as an order parameter for the yielding transition, which sharpens for slow cooling rates and in large systems.

PACS numbers: 62.20.-x, 63.50.Lm 64.70.kj 64.70.pe

## I. INTRODUCTION

Glass formation occurs in many different materials, spanning an enormous range of length scales, including atomic alloys, organic compounds, ceramics, and dense colloidal suspensions [1, 2]. In particular, metallic glasses have received significant attention recently for their promise in technological applications [3–6] that utilize their unique combination of properties (*e.g.* high strength and elasticity) and processability [7–9].

Glasses are often generated by cooling a system in the liquid state sufficiently rapidly such that crystallization is avoided and the system remains disordered at low temperatures [10]. The mechanical response of glasses to applied stress is complex, including strain hardening [11], plastic yielding [12–17], and brittle failure [18–20], and the particular response that is observed for a given glass sample depends on the protocol used to prepare and characterize it (*e.g.* its thermal history) [21]. The cooling rate determines the fictive temperature, which quantifies the degree of structural relaxation that has occurred

during the thermal quench [22–24]. The fictive temperature significantly affects mechanical properties, such as the ductility [20, 25–29], shear band formation [30], quality factor of vibrations [5], and the relation between stress versus strain under quasistatic compression or tension [31, 32].

The fictive temperature defines the average energy of glasses in the potential energy landscape (PEL) [10, 33], which gives the potential energy of the system as a function of all of the particle coordinates (and boundary conditions). The PEL has been used recently to describe the Gardner transition, the temperature below which the separations between basins in the landscape becomes fractal [34, 35], super-Arrhenius structural relaxation [36], as well as reversibility and memory encoding during cyclic shear in glasses [37, 38]. Studies have also quantified the width and depth of basins in the PEL using thermal activation and saddle-point identification methods [39, 40]. This prior work showed that the size of basins are smaller for more rapidly cooled glasses, while asserting that the curvature of the basins is insensitive to

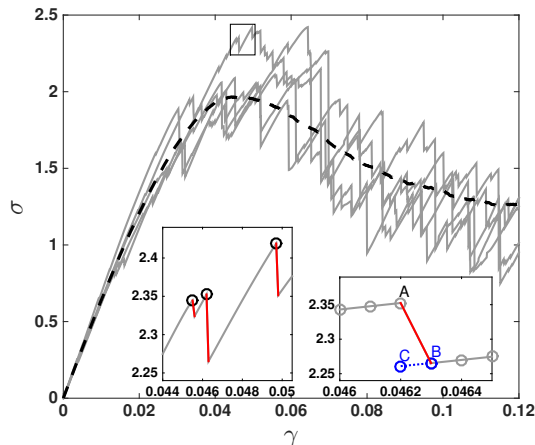


Figure 1: The von Mises stress  $\sigma$  versus strain  $\gamma$  for five glass samples (dark gray curves) with  $N = 2000$  particles prepared at cooling rate  $R = 10^{-4}$  undergoing AQS pure shear. The ensemble-averaged stress  $\langle\sigma\rangle$  over 500 independent samples is shown as the black dashed curve. The left inset provides a close-up of the stress in the strain interval 0.0440 to 0.0505, highlighting three of the stress drops with open circles at the start of the drop and red lines following the drop. The right inset is a close-up of the middle stress drop in the left inset. The gray solid line indicates forward shear increments of  $\delta\gamma = 10^{-4}$ , *i.e.* from point A at  $\gamma = 0.0462$  to point B at  $\gamma + \delta\gamma = 0.0463$ . The blue dotted line indicates backward shear from point B at  $\gamma + \delta\gamma = 0.0463$  to point C at  $\gamma = 0.0462$ . The magnitude of the shear stress difference for this rearrangement is  $|\Delta\sigma(\gamma)| = |\sigma_A - \sigma_C|$  at  $\gamma = 0.0462$ .

the cooling rate. Other computational studies have applied external shear to study the evolution of the system as the PEL deforms with strain [41–44], which strongly influences the mechanical response of glasses. Instead of focusing on small strain intervals near mechanical instabilities, in this work, we will map out the full PEL in the strain direction.

In contrast to crystalline materials, where the creation of and interaction between topological defects controls the mechanical response, it is more difficult to identify the structural defects that control the mechanical response of glasses. In glasses, strong non-affine motion in response to deformation is concentrated in “shear transformation zones” (STZs) [45–47]. Researchers have observed that particles occurring in STZs correlate with those that possess low local yield stress [48] and participate in soft modes defined from the vibrational density of states [49, 50]. These prior studies have shown that with increasing applied shear, the density of STZs increases, the elastic regions decrease in size, STZs percolate, and plastic deformation occurs [51]. Thus, rearrangements and non-affine motion in STZs also strongly impact mechanical response.

In this article, we perform computer simulations of model structural (binary Lennard-Jones) glasses undergoing athermal, quasistatic (AQS) pure shear [43] to

study their mechanical response as a function of the cooling rate used to prepare them. In Fig. 1, we show the shear stress versus strain during AQS pure shear for five glass samples, all prepared at the same cooling rate. While the ensemble-averaged shear stress versus strain is smooth, the curve for each individual sample is not [52]. The left inset of Fig. 1 shows that the shear stress versus strain curve for a single configuration is composed of many nearly linear segments punctuated by stress drops over narrow strain intervals. Similar behavior occurs for the total potential energy per particle  $U$  (and other quantities) versus strain, except in the case of  $U$ , the segments are portions of parabolas. During the strain intervals with continuous variation of  $\sigma$  or  $U$ , the system remains in a series of related minima in the PEL. At the strains corresponding to the stress drops, the system becomes unstable, particles rearrange, and the system evolves to a new lower minimum in the PEL [41–43].

Thus, it is clear that the highly nonlinear shape of the ensemble-averaged stress, potential energy, and other quantities versus strain are determined by 1) the statistics of particle rearrangements including both the frequency and size of rearrangements and 2) changes in the form of the continuous regions of the piecewise curves (*i.e.* softening or a decrease in the slopes of stress versus strain) between rearrangements. There have been a number of previous computational studies focusing on either particle rearrangements [12, 13, 25, 53], or softening of the shear modulus [52, 54] of binary Lennard Jones glasses under applied deformation. In this article, we will study *both* and compare the relative contributions from particle rearrangements and softening in determining the ensemble-averaged nonlinear mechanical response of sheared glasses as a function of the cooling rate used to prepare them.

Note that for much more rapidly cooled glasses than those shown in Fig. 1, strain hardening can occur during AQS pure shear in which the shear stress increases after a rearrangement and/or the slopes of the continuous regions of shear stress increase with strain. Here, we will focus on the cooling-rate regime where strain *softening* behavior is dominant.

We seek to understand the highly nonlinear behavior of the ensemble-averaged stress  $\langle\sigma\rangle$  and potential energy  $\langle U\rangle$  versus strain (Fig. 1). Being able to explain the *ensemble-averaged* mechanical response is important for several reasons. First, we will show below that the system size dependence of ensemble-averaged quantities (like  $\langle\sigma\rangle$  and  $\langle U\rangle$ ) is weak even for modest system sizes. This result suggests that the ensemble average is similar to the spatial average in the large system limit. Second, the magnitude of the particle rearrangements decreases and the frequency of particle rearrangements increases with increasing system size [12]. Thus, it becomes increasingly difficult to distinguish the continuous regions in the mechanical response from drops due to particle rearrangements in large systems.

As shown in Fig. 1, as the applied shear strain in-

creases, the ensemble-averaged stress  $\langle\sigma\rangle$  becomes non-linear in strain, the stress reaches a peak, and then decreases to a plateau value in the large-strain limit. In the strain interval between the strain at which the slope of the stress versus strain curve begins to deviate significantly from that at zero strain and the steady-state strain regime, yielding occurs and the system transitions from an amorphous solid to a liquid-like state that can sample many different configurations. However, it is difficult to precisely define the yielding transition from the smooth, ensemble-averaged stress versus strain  $\langle\sigma(\gamma)\rangle$  [55]. There are many fundamental questions concerning yielding in glasses since it involves a transition between two disordered states. For example, does yielding represent a phase transition and, if so, what is the appropriate order parameter that characterizes the transition [13]?

Recent studies of the system-size scaling of particle rearrangement statistics [12, 13], configurational overlap between minima in the PEL [14], changes in symmetry of nearest-neighbor structure [15], diffusivity of rearranging particles [16], and onset of irreversibility during cyclic shear [17, 37, 55], have suggested that yielding in glassy materials can be described as a non-equilibrium first-order phase transition. For example, the rearrangement frequency displays power-law scaling with system size, with a scaling exponent that changes strongly as the strain approaches the yield strain [13]. Beyond the yield strain, the exponent reaches a plateau value that is independent of the cooling rate. These studies have also shown that the yielding transition becomes less sharp with increasing cooling rate [13]. However, much more work is needed to fully understand the cooling-rate dependence of the rearrangement- and softening-induced losses near yielding.

We present several key results in this study. First, we show that the loss in stress from rearrangements is dominant over the softening-induced stress loss, both of which have different cooling rate and strain dependence. Second, we quantify the rearrangement- and softening-induced potential energy loss as a function of cooling rate and strain. We measure the geometric features of the basins in the PEL along the strain direction and find that the features of the PEL change dramatically near yielding. Third, we propose additional order parameters for the yielding transition based on the stress or energy loss per strain from rearrangements and softening. The stress (or energy) loss per strain increases rapidly near yielding and increasing the system size leads to a sharper transition. Finally, we calculate the distribution of energy drops from rearrangements as a function of strain for different cooling rates. We find that the distribution of energy drops is exponential with an energy scale that also changes dramatically near yielding.

The remainder of the article is organized as follows. In Sec. II, we describe the computer simulations used to prepare and shear the glasses at zero temperature, the physical quantities that will be measured during the applied shear, and the method employed to decompose the shear

stress and potential energy losses into contributions from rearrangements and from softening. Sec. III presents the results from the stress and energy loss decompositions. We also characterize the geometric features of PEL basins along the strain direction. In addition, we identify quantities that change significantly with strain near yielding and assess system-size effects. In Sec. IV, we present our conclusions and describe promising future research directions concerning sheared glasses. In Appendix A, we describe correlations between local structural quantities (such as the local density and composition) and particle rearrangements.

## II. METHODS

Our computational studies focus on model binary Lennard-Jones mixtures, which have been shown to be good glass-formers. The computer simulations are carried out in three stages: 1) Initialization of the liquid state; 2) Cooling the liquid state to a zero-temperature glass at a given rate and fixed low pressure; and 3) Application of AQS pure shear deformation.

We first perform molecular dynamics (MD) simulations of binary Lennard-Jones liquids in three dimensions under periodic boundary conditions with constant particle number  $N$  and pressure  $P$ . We consider 80% large (type  $A$ ) and 20% small (type  $B$ ) spherical particles by number (both with mass  $m$ ) in a cubic box with volume  $V$ . The particles interact pairwise via the shifted-force version of the Lennard-Jones potential,  $u(r_{ij}) = 4\epsilon_{ij}[(\sigma_{ij}/r_{ij})^{12} - (\sigma_{ij}/r_{ij})^6]$  with a cutoff distance  $r_c = 2.5\sigma_{ij}$ , where  $r_{ij}$  is the separation between particles  $i$  and  $j$ . The energy and length parameters follow the Kob-Andersen mixing rules [56]:  $\epsilon_{AA} = 1.0$ ,  $\epsilon_{BB} = 0.5$ ,  $\epsilon_{AB} = 1.5$ ,  $\sigma_{AA} = 1.0$ ,  $\sigma_{BB} = 0.88$ , and  $\sigma_{AB} = 0.8$ . Length, energy, temperature, pressure, and time scales are expressed in units of  $\sigma_{AA}$ ,  $\epsilon_{AA}$ ,  $\epsilon_{AA}/k_B$ ,  $\epsilon_{AA}/\sigma_{AA}^3$ , and  $\sigma_{AA}\sqrt{m/\epsilon_{AA}}$ , respectively, where  $k_B$  is Boltzmann's constant [57]. We considered systems with  $N = 250, 500, 1000, 2000$ , and 4000 particles to study system-size effects.

To set the temperature and pressure, we incorporate a Nosé-Hoover thermostat and barostat and integrate the equations of motion using a second-order symplectic integration scheme [58, 59] with time step  $\Delta t = 10^{-3}$ . We first equilibrate systems in the liquid regime at constant temperature  $T_0 = 0.6$  (larger than the glass transition temperature  $T_g \sim 0.4$  [60]) and pressure  $P = 0.025$  with randomized initial particle positions and velocities. We then cool the systems into a glassy state at zero temperature using a linear cooling ramp,  $T(t) = T_0 - Rt$ , over a range of cooling rates from  $R = 10^{-1}$  to  $10^{-6}$ , all of which are above the critical cooling rate to ensure all zero-temperature samples are disordered. For each cooling rate, we consider at least  $N_c = 500$  configurations with random initial conditions.

After generating each zero-temperature glass, we ap-

ply AQS pure shear at fixed pressure. For each strain step, we expand the box length and move all particles affinely in the  $x$ -direction by a small strain increment  $\delta\gamma_x = \delta\gamma = 10^{-4}$  and compress the box length and move all particles affinely in the  $y$ -direction by the same strain increment  $\delta\gamma_y = -\delta\gamma$ . Following each strain step, we minimize the total enthalpy  $H = \mathcal{U} + PV$  at fixed volume  $V$ , where  $\mathcal{U} = \sum_{i>j} u(r_{ij})$  is the total potential energy. We then either compress or expand the system in the  $z$ -direction to move the system toward the target pressure  $P_0 = 10^{-8}$ . The enthalpy minimization process and scaling of the system in the  $z$ -direction are repeated until the pressure  $P$  is sufficiently close to  $P_0$  with  $|P - P_0|/P_0 < 10^{-4}$ . Additional details concerning the AQS pure shear algorithm can be found in our previous studies [25].

We monitor the total potential energy per particle  $U(\gamma) = \mathcal{U}(\gamma)/N$  and von Mises stress  $\sigma(\gamma)$  as a function of strain  $\gamma$  during the pure shear deformation. The  $3 \times 3$  stress tensor is given by

$$\Sigma_{\mu\delta} = \frac{1}{V} \sum_{i>j} f_{ij\mu} r_{ij\delta}, \quad (1)$$

where  $f_{ij\mu}$  is the  $\mu = x, y, z$  component of the pairwise force  $\vec{f}_{ij}$  that particle  $j$  exerts on particle  $i$ , and  $r_{ij\delta}$  is the  $\delta = x, y, z$  component of the center-to-center distance vector  $\vec{r}_{ij}$  between particles  $i$  and  $j$ . The von Mises stress  $\sigma$  is the second invariant of the stress tensor:

$$\sigma = \sqrt{\frac{3}{2} \text{Tr}(\Sigma + P\mathbf{I})^2}, \quad (2)$$

where  $\mathbf{I}$  is the identity tensor and  $P = -\text{Tr}\Sigma/3$  is the pressure [31]. We subtract the residual stress tensor  $\Sigma(\gamma = 0)$  from  $\Sigma(\gamma)$  so that the von Mises stress  $\sigma(\gamma)$  is initialized to zero at  $\gamma = 0$ .

As described in Sec. I, nonlinearity in ensemble-averaged quantities, such as  $\langle U(\gamma) \rangle$  and  $\langle \sigma(\gamma) \rangle$ , is caused by particle rearrangements and changes to the forms of the piecewise segments of  $U(\gamma)$  and  $\sigma(\gamma)$  between rearrangements. We analyze the relative contributions of the two effects by defining:

$$\sigma(\gamma) = \sigma_{\text{elastic}}(\gamma) - \sigma_{\text{loss}}^r(\gamma) - \sigma_{\text{loss}}^s(\gamma), \quad (3)$$

where  $\sigma_{\text{elastic}}(\gamma)$  is the stress in the absence of losses from rearrangements and softening,  $\sigma_{\text{loss}}^r(\gamma)$  is the loss in stress from particle rearrangements, and  $\sigma_{\text{loss}}^s(\gamma)$  is the loss in stress from softening. We define a similar expression for the total potential energy per particle:

$$U(\gamma) = U_{\text{elastic}}(\gamma) - U_{\text{loss}}^r(\gamma) - U_{\text{loss}}^s(\gamma), \quad (4)$$

where  $U_{\text{elastic}}(\gamma)$  is potential energy in the absence of losses from rearrangements and softening, and  $U_{\text{loss}}^r(\gamma)$  and  $U_{\text{loss}}^s(\gamma)$  give the potential energy loss from rearrangements and softening, respectively.

In previous simulation studies of AQS pure shear [25], we developed a method to unambiguously determine

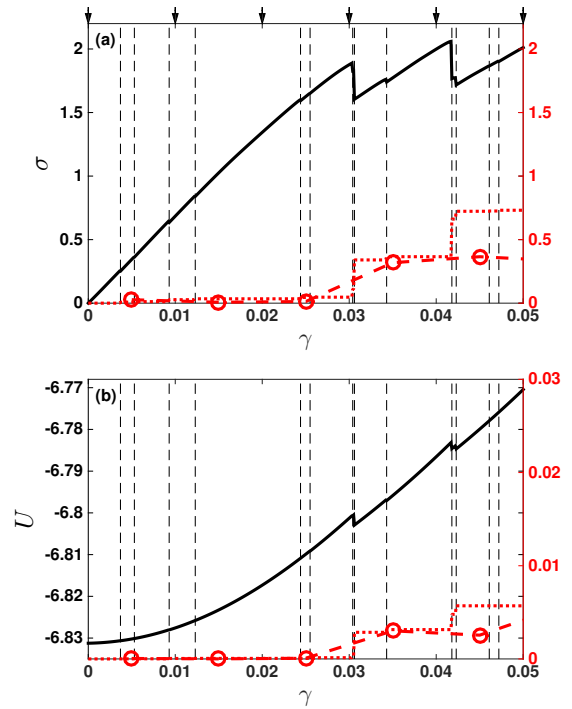


Figure 2: Method to quantify the rearrangement-induced stress and energy losses. (a) The von Mises stress  $\sigma$  and (b) total potential energy per particle  $U$  plotted versus strain  $\gamma$  (solid black curves) for a single glass configuration prepared at  $R = 10^{-4}$  undergoing AQS pure shear. The vertical dashed lines indicate the strains at which rearrangements occur. The rearrangement-induced cumulative stress loss  $\sigma_{\text{loss}}^r$  (Eq. 5) and potential energy loss  $U_{\text{loss}}^r$  (Eq. 6) are shown by the red dotted curves, with tick marks on the right vertical axis. The binned rearrangement-induced stress and energy loss per (1%) strain,  $d\sigma_{\text{loss}}^r/d\gamma$  (Eq. 7) and  $dU_{\text{loss}}^r/d\gamma$  (Eq. 8), are indicated by red circles and dashed lines with tick marks on the right vertical axis. The strain dependence has been binned with width  $d\gamma = 0.01$ ; the edges of each bin are indicated by black arrows in panel (a).

whether a particle rearrangement event occurs during the strain interval  $\gamma$  to  $\gamma + \delta\gamma$  with an accuracy on the order of numerical precision. We denote the total number of rearrangements in the strain interval 0 to  $\gamma$  as  $N_r(\gamma)$ . We calculate the cumulative rearrangement-induced stress and energy loss after the  $N_r(\gamma)$  rearrangements in the strain interval 0 to  $\gamma$  as:

$$\sigma_{\text{loss}}^r(\gamma) = \sum_{i=1}^{N_r(\gamma)} |\Delta\sigma(\gamma_i)| \quad (5)$$

$$U_{\text{loss}}^r(\gamma) = \sum_{i=1}^{N_r(\gamma)} |\Delta U(\gamma_i)|, \quad (6)$$

where  $\gamma_i$  indicates the strains at which rearrangements occur and  $\Delta\sigma(\gamma_i)$  and  $\Delta U(\gamma_i)$  are the stress and potential energy drops at each rearrangement, respectively.

(See the right inset of Fig. 1.) We also measure the rearrangement-induced stress and potential energy losses per strain:

$$\left[ \frac{d\sigma_{\text{loss}}^r}{d\gamma} \right] (\gamma) = \frac{\sigma_{\text{loss}}^r(\gamma + d\gamma) - \sigma_{\text{loss}}^r(\gamma)}{d\gamma} \quad (7)$$

$$\left[ \frac{dU_{\text{loss}}^r}{d\gamma} \right] (\gamma) = \frac{U_{\text{loss}}^r(\gamma + d\gamma) - U_{\text{loss}}^r(\gamma)}{d\gamma}, \quad (8)$$

using bins of width  $d\gamma = 10^{-2}$ . The stress and potential energy losses from rearrangements ( $\sigma_{\text{loss}}^r$  and  $U_{\text{loss}}^r$ ), as well as the corresponding losses per strain ( $d\sigma_{\text{loss}}^r/d\gamma$  and  $dU_{\text{loss}}^r/d\gamma$ ), are shown in Fig. 2 for a single configuration prepared at  $R = 10^{-4}$ .

In Fig. 3, we illustrate how we quantify the effect of softening on  $\sigma(\gamma)$  and  $U(\gamma)$ . In panel (a), we show  $\sigma(\gamma)$  for a single configuration as open circles over a small strain interval.  $\sigma(\gamma)$  is nearly linear in regions of strain between the three stress drops that are indicated by dashed vertical lines. We define the stress loss per strain from softening as:

$$\left[ \frac{d\sigma_{\text{loss}}^s}{d\gamma} \right] (\gamma) = G_0 - G(\gamma), \quad (9)$$

where  $G_0$  is the slope of  $\sigma(\gamma)$  in the  $\gamma = 0$  limit (solid black line in Fig. 3 (a)) and  $G(\gamma)$  is the slope of  $\sigma(\gamma)$  at strain  $\gamma$  (solid blue lines in Fig. 3 (a)).  $d\sigma_{\text{loss}}^s/d\gamma$  is a constant for each piecewise linear stress-strain segment and is discontinuous at rearrangements. We also measure the cumulative softening-induced stress loss for strain up to  $\gamma$  by integrating the corresponding stress loss per strain:

$$\sigma_{\text{loss}}^s(\gamma) = \int_0^\gamma (d\sigma_{\text{loss}}^s/d\gamma') d\gamma', \quad (10)$$

which is continuous, but the slope of the curve changes discontinuously at each rearrangement.

To quantify the effect of softening on the potential energy versus strain  $U(\gamma)$  (Fig. 3 (b)), we find the best-fit parabola for each piecewise elastic segment between rearrangement events using

$$U(\gamma) = \frac{A}{2}\gamma^2 + B\gamma + C, \quad (11)$$

where  $A$ ,  $B$ , and  $C$  are coefficients that determine the concavity and location of the parabola. We define the potential energy loss per strain from softening as  $dU_{\text{loss}}^s/d\gamma = k_0 - k(\gamma)$ , where  $k_0$  and  $k$  are the local slopes of  $U(\gamma)$  at strains 0 and  $\gamma$ , respectively. Using Eq. 11, we define the softening-induced potential energy loss per strain as:

$$\left[ \frac{dU_{\text{loss}}^s}{d\gamma} \right] (\gamma) = (A_0 - A(\gamma))\gamma + B_0 - B(\gamma), \quad (12)$$

where the coefficients  $A_0$  and  $B_0$  are measured at  $\gamma = 0$ . In contrast to  $d\sigma_{\text{loss}}^s/d\gamma$ , which is constant,  $dU_{\text{loss}}^s/d\gamma$  depends linearly on  $\gamma$  for each inter-rearrangement segment.

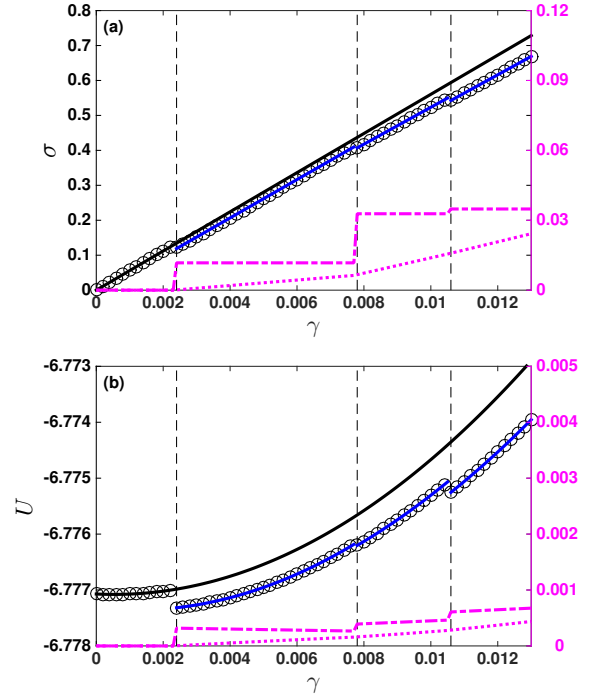


Figure 3: Method to quantify the softening-induced stress and energy losses. (a) The von Mises stress  $\sigma$  and (b) total potential energy per particle  $U$  plotted versus strain  $\gamma$  (open black circles) for a single glass configuration prepared at  $R = 10^{-2}$  undergoing AQS pure shear. Three rearrangements (indicated by dashed vertical lines) occur in the strain interval  $0 < \gamma < 0.014$ . In (a), the regions of  $\sigma(\gamma)$  between each rearrangement are nearly linear. Best-fit blue lines are shown for each segment. The solid black line has slope  $G_0$  representing the slope of  $\sigma(\gamma)$  near  $\gamma = 0$ . The stress loss per (1%) strain ( $d\sigma_{\text{loss}}^s/d\gamma$ ) arising from changes in the slope of the line segments (magenta dot-dashed curve with tick labels on the right vertical axis) and the corresponding cumulative stress loss  $\sigma_{\text{loss}}^s$  (magenta dotted curve with tick labels on the right vertical axis) are also shown. In (b), the regions of  $U(\gamma)$  between each rearrangement are parabolic. The best-fit parabolas (blue curves) for each strain interval are shown. The solid black curve is the best-fit parabola  $U_0(\gamma)$  for the potential energy near  $\gamma = 0$ . The potential energy loss per (1%) strain  $dU_{\text{loss}}^s/d\gamma$  arising from changes in the local slope of  $U(\gamma)$  (magenta dot-dashed curve with tick marks on the right vertical axis) and the cumulative potential energy loss  $U_{\text{loss}}^s$  (magenta dotted curve with tick marks on the right vertical axis) are also shown.

The cumulative softening-induced potential energy loss can be calculated by integrating  $dU_{\text{loss}}^s/d\gamma$  over a given strain interval:

$$U_{\text{loss}}^s(\gamma) = \int_0^\gamma (dU_{\text{loss}}^s/d\gamma') d\gamma'. \quad (13)$$

$U_{\text{loss}}^s(\gamma)$  is piecewise quadratic, whereas  $\sigma_{\text{loss}}^s(\gamma)$  is piecewise linear.

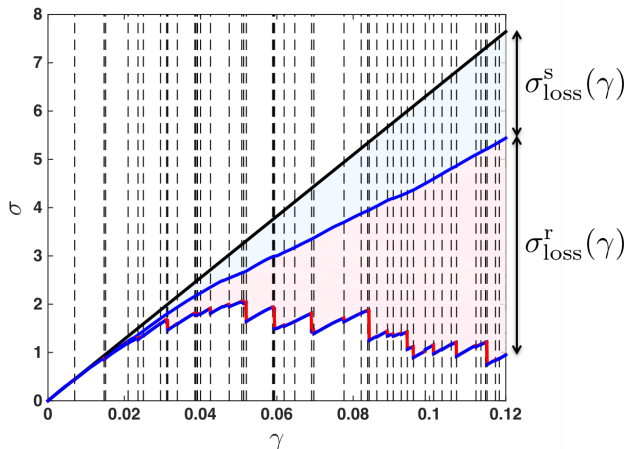


Figure 4: Rearrangement and softening effects on the von Mises stress  $\sigma$  for a single glass configuration (with  $N = 2000$  and  $R = 10^{-4}$ ) undergoing AQS pure shear.  $\sigma(\gamma)$  (bottom curve) has nearly linear continuous segments (blue lines) punctuated by rapid stress drops caused by particle rearrangements (red lines). The strains at which the rearrangements occur are indicated by dashed vertical lines. The middle blue solid curve is obtained by connecting the continuous segments of  $\sigma(\gamma)$  between rearrangements end to end. The stress  $\sigma_{\text{elastic}}$  in the absence of rearrangements and softening (top black line) is obtained from the slope of  $\sigma(\gamma)$  in the  $\gamma \rightarrow 0$  limit. The cumulative rearrangement-induced stress loss  $\sigma_{\text{loss}}^r(\gamma)$  (Eq. 5) is defined as the width of the red-shaded region at each strain  $\gamma$ . The cumulative softening-induced stress loss  $\sigma_{\text{loss}}^s(\gamma)$  (Eq. 6) is defined as the width of the blue-shaded area at each strain  $\gamma$ .

### III. RESULTS

The discussion of the results is organized into three subsections. First, in Sec. 3.1, we illustrate the effects of rearrangements and softening on the ensemble-averaged stress versus strain curve as a function of the cooling rate. In particular, we compare the relative contributions of rearrangements and softening to the nonlinear mechanical response. In Sec. 3.2, we identify the distinct contributions of rearrangements and softening to the loss in potential energy as a function of strain. In addition, we study the properties of the parabolic segments of  $U(\gamma)$  between rearrangements to characterize the width and height of basins in the PEL near the yielding transition. In Sec. 3.3, we investigate the system-size scaling exponents for the size and frequency of rearrangements and the distribution of energy drops from rearrangements near the yielding transition. In addition, we study the stress and energy losses from rearrangements and softening as a function of system size.

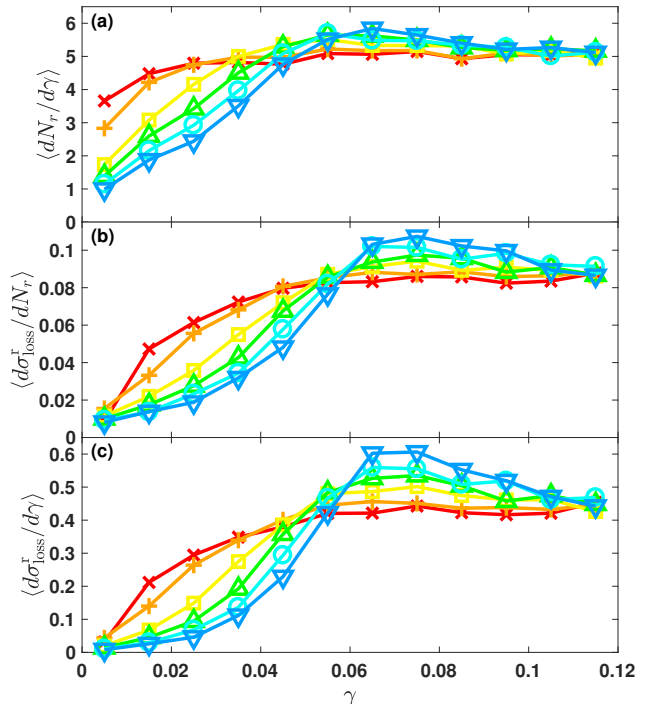


Figure 5: Ensemble-averaged (a) rearrangement frequency  $\langle dN_r/d\gamma \rangle$ , (b) stress loss per rearrangement  $\langle d\sigma_{\text{loss}}^r/dN_r \rangle$ , and (c) rearrangement-induced stress loss per (1%) strain  $\langle d\sigma_{\text{loss}}^r/d\gamma \rangle$  plotted versus strain  $\gamma$  for glasses undergoing AQS pure shear. The glasses were prepared using cooling rates  $R = 10^{-1}$  (crosses),  $10^{-2}$  (plus signs),  $10^{-3}$  (squares),  $10^{-4}$  (upward triangles),  $10^{-5}$  (circles), and  $10^{-6}$  (downward triangles). All data is obtained by averaging over 500 independent samples with  $N = 2000$ .

#### 3.1. Stress losses from rearrangements and softening

In Fig. 4, we show the von Mises stress versus strain  $\sigma(\gamma)$  for a single glass configuration with  $N = 2000$  prepared at  $R = 10^{-4}$  undergoing AQS pure shear. We identify the elastic contribution to the stress  $\sigma_{\text{elastic}}(\gamma)$  in the absence of rearrangements and softening, the stress loss from rearrangements  $\sigma_{\text{loss}}^r(\gamma)$ , and the stress loss from softening  $\sigma_{\text{loss}}^s(\gamma)$ . We find that both  $\sigma_{\text{loss}}^r(\gamma)$  and  $\sigma_{\text{loss}}^s(\gamma)$  increase with strain. For most configurations including this one, the stress loss from rearrangements is larger than that from softening,  $\sigma_{\text{loss}}^r(\gamma) > \sigma_{\text{loss}}^s(\gamma)$ , and the difference grows with increasing strain.

The stress loss per strain  $d\sigma_{\text{loss}}^r/d\gamma$  from rearrangements (Eq. 7) can be decomposed as  $d\sigma_{\text{loss}}^r/d\gamma = (d\sigma_{\text{loss}}^r/dN_r)(dN_r/d\gamma)$ , where  $dN_r/d\gamma$  is the rearrangement frequency (*i.e.*, number of rearrangements per strain) and  $d\sigma_{\text{loss}}^r/dN_r$  is the rearrangement size (*i.e.*, stress loss per rearrangement). In Fig. 5, we show the ensemble average of all three quantities,  $\langle dN_r/d\gamma \rangle$ ,  $\langle d\sigma_{\text{loss}}^r/dN_r \rangle$ , and  $\langle d\sigma_{\text{loss}}^r/d\gamma \rangle$ , for glasses prepared over a range of cooling rates. We find that all three increase

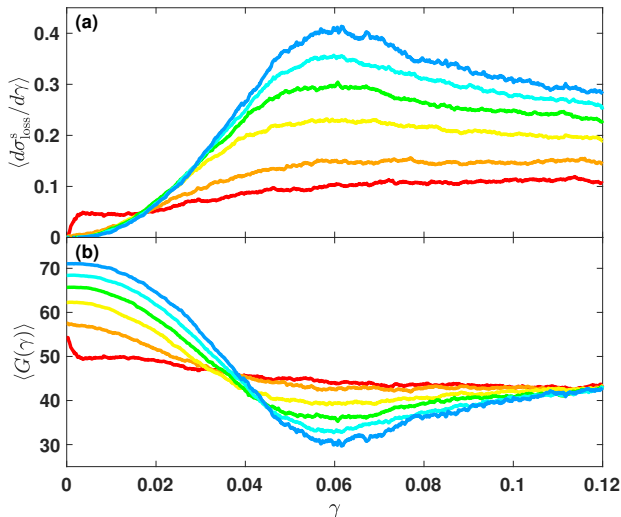


Figure 6: Ensemble-averaged (a) softening-induced stress loss per (1%) strain  $\langle d\sigma_{\text{loss}}^s/d\gamma \rangle$  and (b) local slope of the continuous stress versus strain segments  $\langle G(\gamma) \rangle$  plotted versus strain  $\gamma$  for cooling rates  $R = 10^{-1}$  (red),  $10^{-2}$  (orange),  $10^{-3}$  (yellow),  $10^{-4}$  (green),  $10^{-5}$  (cyan), and  $10^{-6}$  (blue). All data is obtained by averaging over 500 configurations with  $N = 2000$ .

at small strains ( $\gamma \lesssim 0.05$ ), plateau at large strains ( $\gamma \gtrsim 0.1$ ), and form a peak in the intermediate strain regime ( $0.05 \lesssim \gamma \lesssim 0.1$ ). The peaks are more prominent for  $\langle d\sigma_{\text{loss}}^r/dN_r \rangle$  and  $\langle d\sigma_{\text{loss}}^r/d\gamma \rangle$ . At small strains, all three quantities increase with cooling rate, indicating that rearrangements play a more significant role in stress loss in more rapidly cooled glasses. In contrast, at intermediate strains, all three quantities decrease with increasing cooling rate. In the large strain regime, none of the quantities show cooling rate dependence.

In Fig. 6 (a), we show the ensemble-averaged softening-induced stress loss per strain,  $\langle d\sigma_{\text{loss}}^s/d\gamma \rangle$  (Eq. 9).  $\langle d\sigma_{\text{loss}}^s/d\gamma \rangle$  increases at small strains and plateaus at cooling rate-dependent values at large strains. In the intermediate strain regime,  $\langle d\sigma_{\text{loss}}^s/d\gamma \rangle$  is larger for more slowly cooled glasses with a pronounced peak. To gain insight into this behavior, we plot the ensemble-averaged slope of the continuous stress versus strain segments  $\langle G(\gamma) \rangle$  in Fig. 6 (b). At  $\gamma = 0$ , the shear modulus  $\langle G(0) \rangle$  depends on the degree of heterogeneity in the material and thus increases with decreasing  $R$  [32]. As  $\gamma$  increases,  $\langle G(\gamma) \rangle$  decreases at small strains and reaches a plateau value ( $\approx 40$ ) at large strains that is independent of cooling rate. In the intermediate strain regime, for slowly cooled glasses, *e.g.*  $R = 10^{-6}$ ,  $\langle G(\gamma) \rangle$  first decreases near  $\gamma \approx 0.04$  and reaches a minimum near  $\gamma \approx 0.06$  corresponding to the peak in  $\langle d\sigma_{\text{loss}}^s/d\gamma \rangle$ . Thus, at small strains, the slowly cooled glasses are the most rigid, while at intermediate strains, they are the least rigid. For rapidly cooled glasses, the non-monotonic behavior in strain is absent and the shear modulus  $\langle G(\gamma) \rangle$  decreases continuously with strain until it plateaus in the large-strain limit.

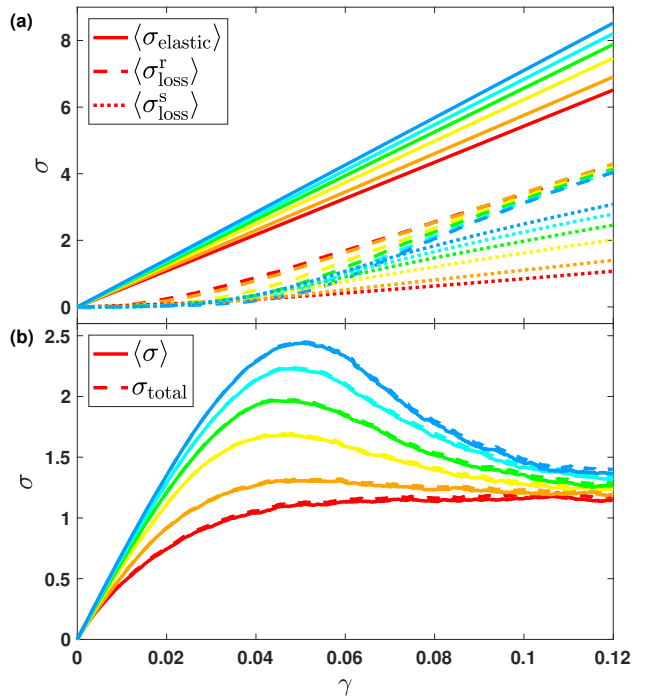


Figure 7: Ensemble-averaged (a) elastic stress  $\sigma_{\text{elastic}}(\gamma)$  (solid), rearrangement-induced stress loss  $\sigma_{\text{loss}}^r(\gamma)$  (dashed), and softening-induced stress loss  $\sigma_{\text{loss}}^s(\gamma)$  (dotted) plotted versus strain  $\gamma$ . (b) Ensemble-averaged stress  $\langle \sigma(\gamma) \rangle$  and the stress  $\sigma_{\text{total}}$  obtained by combining the elastic stress, and the rearrangement- and softening-induced stress losses (Eq. 3) plotted versus  $\gamma$ . In both (a) and (b), the system size  $N = 2000$ , and six cooling rates,  $R = 10^{-1}$  (red),  $10^{-2}$  (orange),  $10^{-3}$  (yellow),  $10^{-4}$  (green),  $10^{-5}$  (cyan), and  $10^{-6}$  (blue) are shown.

To compare the relative contributions of rearrangements and softening on the stress loss, we integrate  $d\sigma_{\text{loss}}^r/d\gamma$  and  $d\sigma_{\text{loss}}^s/d\gamma$  over strain to obtain the cumulative stress losses,  $\sigma_{\text{loss}}^r$  and  $\sigma_{\text{loss}}^s$ , respectively. In Fig. 7, we show the ensemble average of the four variables in Eq. 3, as well as the direct ensemble average  $\langle \sigma(\gamma) \rangle$  of stress from single glass configurations, for different cooling rates  $R$ . The ensemble-averaged stress versus strain  $\langle \sigma(\gamma) \rangle$  and the combination of the terms in Eq. 3,  $\sigma_{\text{total}}(\gamma)$ , agree quantitatively.

In general,  $\langle \sigma_{\text{loss}}^r \rangle > \langle \sigma_{\text{loss}}^s \rangle$ , which means that stress losses from rearrangements are larger than those from softening. For the sake of discussion, we divide the stress versus strain curve into three regions: the pre-peak region ( $\gamma \lesssim 0.04$ ), the peak region ( $0.04 \lesssim \gamma \lesssim 0.07$ ), and the post-peak region ( $\gamma \gtrsim 0.07$ ). In the pre-peak region, the stress loss from softening  $\langle \sigma_{\text{loss}}^s \rangle$  is extremely small, while the stress loss from rearrangements  $\langle \sigma_{\text{loss}}^r \rangle$  is nonzero and increases for more rapidly cooled glasses. Significant stress loss from rearrangements in the pre-peak region for rapidly cooled glasses explains the strongly nonlinear behavior of the stress versus strain for large cooling rates  $R$ . The ability of rapidly cooled glasses to undergo

rearrangements in the pre-peak strain region is also correlated with enhanced ductility [25]. In the peak region, the stress loss from softening ( $\sigma_{\text{loss}}^{\text{s}}$ ) begins to grow and becomes comparable to the stress loss from rearrangements ( $\sigma_{\text{loss}}^{\text{r}}$ ). However,  $\langle\sigma_{\text{loss}}^{\text{r}}\rangle$  and  $\langle\sigma_{\text{loss}}^{\text{s}}\rangle$  display opposite cooling rate dependence. More rapidly cooled glasses have larger stress loss from rearrangements and smaller stress loss from softening in the peak region. In contrast, more slowly cooled glasses possess smaller stress loss from rearrangements and larger stress loss from softening. In the post-peak region, both  $\langle\sigma_{\text{loss}}^{\text{r}}\rangle$  and  $\langle\sigma_{\text{loss}}^{\text{s}}\rangle$  increase linearly with  $\gamma$ . At large strains, the stress loss from rearrangements ( $\langle\sigma_{\text{loss}}^{\text{r}}\rangle$ ) becomes cooling-rate independent. However, the cooling rate dependence of the stress loss from softening ( $\langle\sigma_{\text{loss}}^{\text{s}}\rangle$ ) increases at large strains. In this region,  $\langle\sigma_{\text{loss}}^{\text{s}}\rangle$  increases for more slowly cooled glasses, which gives rise to the strong decay in  $\langle\sigma(\gamma)\rangle$  at strains beyond the peak stress. (See Fig. 7.)

### 3.2. Losses in potential energy and geometric features of basins in the energy landscape

In this subsection, we will quantify the losses in the potential energy  $U$  from rearrangements and softening during AQS pure shear deformation. In addition, we will characterize the geometric features of basins in the potential energy landscape along the strain direction as a function of the cooling rate  $R$  used to prepare the glasses.

In Fig. 8, we show the ensemble-averaged potential energy  $\langle U(\gamma) \rangle$  and compare the potential energy losses from rearrangements ( $\langle U_{\text{loss}}^{\text{r}}(\gamma) \rangle$ ) and from softening ( $\langle U_{\text{loss}}^{\text{s}}(\gamma) \rangle$ ) as a function of strain. By construction, the direct ensemble-averaged potential energy  $\langle U(\gamma) \rangle$  agrees quantitatively with the potential energy  $U_{\text{total}}(\gamma)$  obtained by combining the terms  $U_{\text{elastic}}(\gamma)$ ,  $U_{\text{loss}}^{\text{r}}(\gamma)$ , and  $U_{\text{loss}}^{\text{s}}(\gamma)$  from Eq. 4. Near  $\gamma = 0$ ,  $\langle U(\gamma) \rangle$  is larger for more rapidly cooled glasses since rapid cooling prevents the system from exploring configuration space and finding lower energy minima [10, 31]. At small strains,  $\langle U(\gamma) \rangle$  increases quadratically for all cooling rates (except for  $R = 10^{-1}$ ) since the losses from rearrangements and softening are small.

As  $\gamma$  increases, the ensemble-averaged potential energy  $\langle U(\gamma) \rangle$  deviates from quadratic behavior due to increases in losses from rearrangements  $U_{\text{loss}}^{\text{r}}(\gamma)$  and softening  $U_{\text{loss}}^{\text{s}}(\gamma)$ . At large strains,  $\langle U(\gamma) \rangle$  approaches a plateau value that is independent of the cooling rate  $R$  [31]. As shown in Fig. 8 (a), the potential energy loss from rearrangements ( $\langle U_{\text{loss}}^{\text{r}}(\gamma) \rangle$ ) increases with cooling rate for all  $\gamma$  [25]. This behavior has been associated with the generation of free volume via shear-induced particle rearrangements [48, 50]. To make contact with these previous studies, we provide a detailed characterization of changes in local properties (such as the local density and composition) after rearrangements in Appendix A. In contrast to the behavior for the stress losses from rearrangements (Fig. 7 (a)), the potential energy loss from

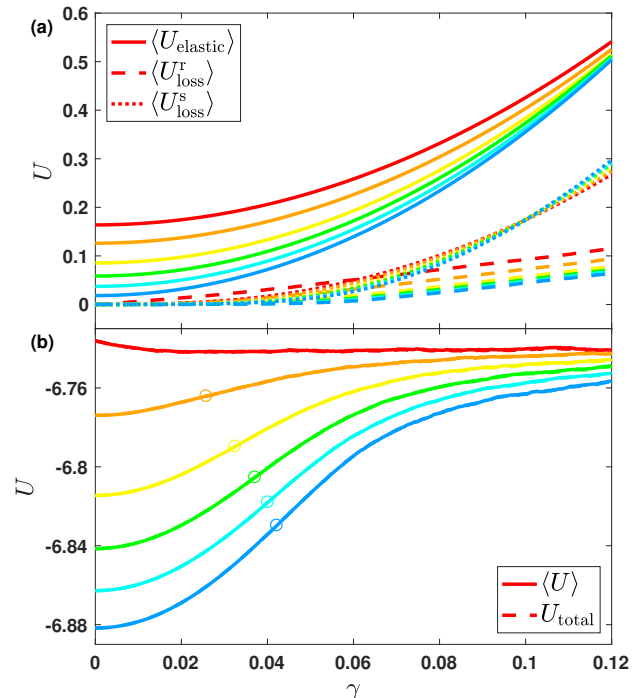


Figure 8: Ensemble-averaged (a) elastic potential energy  $\langle U_{\text{elastic}}(\gamma) \rangle$ , rearrangement-induced potential energy loss  $\langle U_{\text{loss}}^{\text{r}}(\gamma) \rangle$ , and softening-induced potential energy loss  $\langle U_{\text{loss}}^{\text{s}}(\gamma) \rangle$  plotted versus strain  $\gamma$ . (b) Ensemble-averaged potential energy  $\langle U(\gamma) \rangle$  and the potential energy  $U_{\text{total}}(\gamma)$  obtained by combining the elastic energy, and the rearrangement- and softening-induced energy losses (Eq. 4) plotted versus  $\gamma$  for cooling rates  $R = 10^{-1}$  (red),  $10^{-2}$  (orange),  $10^{-3}$  (yellow),  $10^{-4}$  (green),  $10^{-5}$  (cyan), and  $10^{-6}$  (blue). All data is obtained by averaging over 500 samples with system size  $N = 2000$ . The inflection points of  $\langle U(\gamma) \rangle$  are indicated by open circles. Note that  $\langle U(\gamma) \rangle$  reaches a cooling-rate independent plateau value for  $\gamma \gtrsim 0.2$ .

rearrangements ( $\langle U_{\text{loss}}^{\text{r}}(\gamma) \rangle$ ) is smaller than the potential energy loss from softening ( $\langle U_{\text{loss}}^{\text{s}}(\gamma) \rangle$ ). In fact, at large strains,  $\langle U_{\text{loss}}^{\text{s}}(\gamma) \rangle$  grows more rapidly with strain than  $\langle U_{\text{loss}}^{\text{r}}(\gamma) \rangle$ . The strain dependence of  $\langle U_{\text{loss}}^{\text{s}}(\gamma) \rangle$  originates from the evolution with strain of the geometric features of the PEL (*i.e.*, the  $\gamma$ -dependence of the two terms,  $(A_0 - A(\gamma))\gamma$  and  $B_0 - B(\gamma)$ , in Eq. 12), which will be discussed below.

As shown in Fig. 9 (a), the potential energy versus strain  $U(\gamma)$  for a single glass configuration is composed of a series of continuous parabolic segments punctuated by rapid rearrangement-induced drops. Along the continuous segments in strain, the system remains in a series of similar minima in the potential energy landscape. As the strain continues to increase, the potential energy minimum will become unstable, the system will undergo a rearrangement and move to a new minimum. With subsequent increases in strain, the system will follow a new continuous parabolic segment until that energy minimum becomes unstable. In Fig. 9 (b), we define several

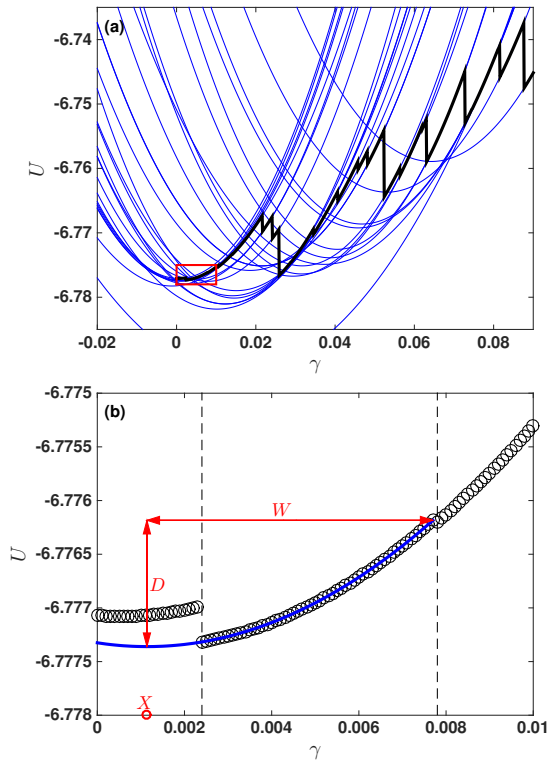


Figure 9: (a) Potential energy  $U$  versus strain  $\gamma$  for a single glass configuration (thick black curve) with  $N = 2000$  and prepared with cooling rate  $R = 10^{-2}$ . The best fit parabolas for each of the continuous segments of  $U(\gamma)$  in the range  $0 < \gamma < 0.09$  are shown as thin blue curves. (b) Close-up of  $U(\gamma)$  in the range  $0 < \gamma < 0.01$  indicated by the red rectangle in panel (a). For this configuration (black circles) and range of strain, two rearrangements occur (indicated by dashed vertical lines). We show the best-fit parabola (solid blue curve) for the continuous segment between the two rearrangements. The half-width  $W$  and depth  $D$  of the basin are indicated by the red arrows. The strain location of the minimum  $\gamma = X$  of the continuous parabolic segment is given by the open circle.

geometric features of the PEL along the strain direction. For each continuous segment of  $U(\gamma)$ , we find the best fit parabola using Eq. 11 with half-width  $W = B/A + \gamma_i$ , depth  $D = U(\gamma_i) - C + B^2/(2A)$ , and strain location of the minimum  $X = -B/A$ , where  $\gamma_i$  is the strain at which a rearrangement occurs (on the large strain side of the continuous segment).

In Fig. 10, we show the ensemble-averaged potential energy landscape parameters  $\langle A \rangle$ ,  $\langle X \rangle$ , and  $\langle B \rangle$  as a function of strain  $\gamma$  and cooling rate  $R$ . Similar to the ensemble-averaged shear modulus  $\langle G \rangle$  in Fig. 6, the concavity  $\langle A \rangle$  depends weakly on  $\gamma$  for rapidly cooled glasses. However,  $\langle A \rangle$  becomes increasingly non-monotonic in  $\gamma$  as the cooling rate decreases. In panel (b), we show that the strain location of the basin minimum occurs at  $\langle X \rangle = 0$  at  $\gamma = 0$ , and  $\langle X \rangle$  either increases with  $\gamma$  (for large  $R$ ) or decreases with  $\gamma$  (for small  $R$ ) depending on the cooling rate. Large deviations from  $\langle X \rangle = 0$  are as-

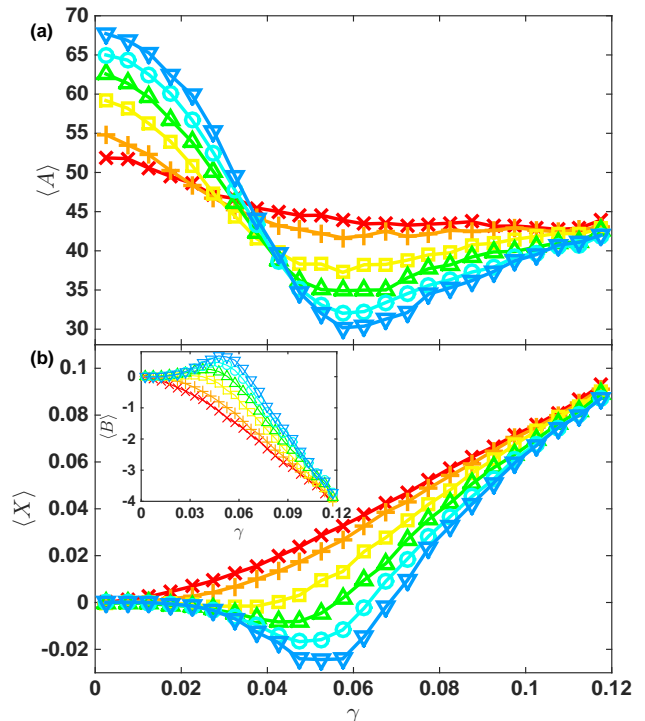


Figure 10: Ensemble-averaged features of the PEL along the strain direction. We plot (a) the concavity  $\langle A \rangle$  and (b) strain location of the potential energy minimum  $\langle X \rangle$  for the continuous segments versus  $\gamma$ . In the inset, we also include  $\langle B \rangle$  versus  $\gamma$  for the continuous segments. For all data, we show six cooling rates,  $R = 10^{-1}$  (crosses),  $10^{-2}$  (plus signs),  $10^{-3}$  (squares),  $10^{-4}$  (upward triangles),  $10^{-5}$  (circles), and  $10^{-6}$  (downward triangles), and average over 500 samples with  $N = 2000$ .

sociated with yielding. For rapidly cooled glasses, there are many nearby minima in the PEL [61] with similar values of  $\langle A \rangle$ ,  $\langle B \rangle < 0$ , and values of  $|\langle B \rangle|$  that increase with strain. Thus, rapidly cooled glasses possess basins with  $\langle X \rangle$  that increase with  $\gamma$ . For more slowly cooled glasses, rearrangements below yielding are less intense (Fig. 5 (c)). In this case,  $\langle B \rangle$  changes signs and  $\langle A \rangle$  decreases with strain near yielding. As a result,  $\langle X \rangle < 0$  for slowly cooled glasses in the strain regime near yielding. At large  $\gamma$ ,  $\langle X \rangle \sim \gamma$  for all cooling rates.

There are two contributions to the potential energy loss  $\langle U_{\text{loss}}^s \rangle$  from softening. The first contribution, from the integration of  $(A_0 - A(\gamma))\gamma$  over strain, is similar to the stress loss from softening  $\langle \sigma_{\text{loss}}^s \rangle$ . The second contribution stems from the integration of  $B_0 - B(\gamma)$  over  $\gamma$ . For rapidly cooled glasses, the second contribution to  $\langle U_{\text{loss}}^s \rangle$  is larger than the first for all strains. For slowly cooled glasses, when  $\langle B(\gamma) \rangle$  becomes sufficiently positive near yielding (inset to Fig. 10 (b)), the second contribution can switch from positive to negative, providing an effective potential energy gain. However, for slowly cooled glasses, the potential energy loss from the first contribution is much larger than the effective gain, and

thus  $\langle U_{\text{loss}}^s(\gamma) \rangle$  also grows with  $\gamma$  for slowly cooled glasses as shown in Fig. 8 (a).

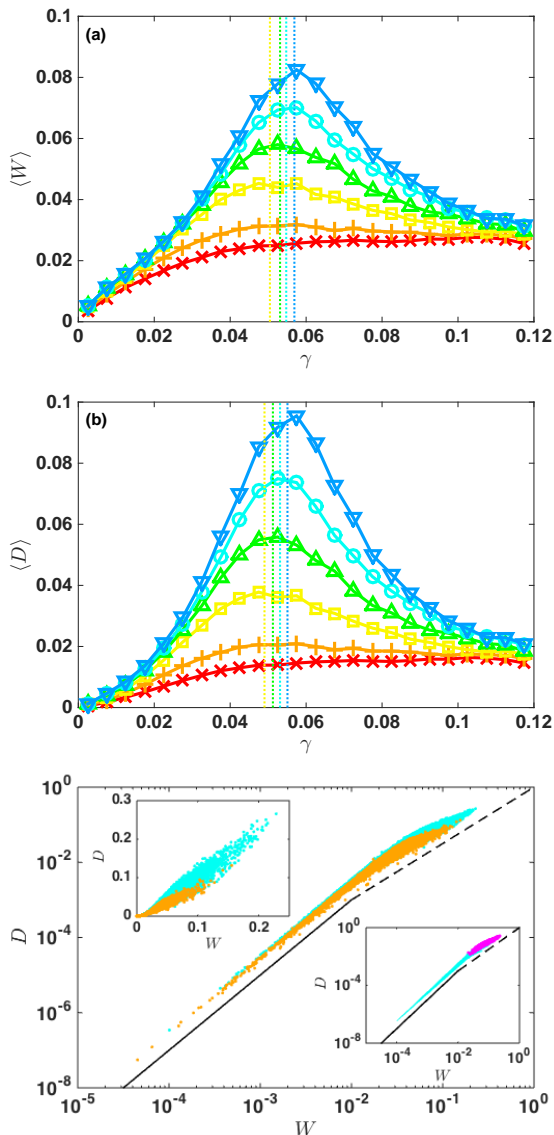


Figure 11: Ensemble-average of (a) the half-width  $\langle W \rangle$  and (b) depth  $\langle D \rangle$  of the continuous segments of the potential energy  $U(\gamma)$  versus the midpoint strain for each segment for cooling rates  $R = 10^{-1}$  (crosses),  $10^{-2}$  (plus signs),  $10^{-3}$  (squares),  $10^{-4}$  (upward triangles),  $10^{-5}$  (circles), and  $10^{-6}$  (downward triangles). The strains  $\gamma^*$  at which  $\langle W \rangle$  and  $\langle D \rangle$  form a peak are indicated by dotted lines for those cooling rates  $R$  where a peak is clearly visible. (c) Scatter plot of  $D$  versus  $W$  for all continuous segments in the strain interval  $0 < \gamma < 0.12$  for  $R = 10^{-2}$  (orange) and  $10^{-5}$  (cyan). The solid and dashed lines have slopes 2 and 1.5, respectively. The upper-left inset shows  $D$  versus  $W$  on a linear-linear scale for  $R = 10^{-2}$  (orange) and  $10^{-5}$  (cyan), and the lower-right inset shows  $D$  versus  $W$  on a  $\log_{10}$ - $\log_{10}$  scale for  $R = 10^{-5}$ . Data near yielding ( $0.045 < \gamma < 0.065$ ) are colored magenta.

We now focus on the strain and cooling rate dependence of the half-width  $W$  and depth  $D$  of the basins

that are sampled in the PEL along the strain direction during AQS pure shear. As shown in Fig. 11 (a) and (b), the ensemble-averaged  $\langle W \rangle$  and  $\langle D \rangle$  possess similar dependence on strain and cooling rate.  $\langle W \rangle = \langle D \rangle = 0$  at  $\gamma = 0$  and then both increase with  $\gamma$  for small strains. As  $\gamma$  continues to increase,  $\langle W \rangle$  and  $\langle D \rangle$  become cooling-rate dependent. For rapidly cooled glasses,  $\langle W \rangle$  and  $\langle D \rangle$  grow monotonically with strain, reaching plateau values ( $\langle W \rangle \sim 0.03$  and  $\langle D \rangle \sim 0.02$ ) in the large-strain limit. In contrast, for slowly cooled glasses,  $\langle W \rangle$  and  $\langle D \rangle$  form peaks near  $\gamma^* \sim 0.055$  before reaching their large-strain plateau values. The values of  $\gamma^*$  for slowly cooled glasses are similar to those for the peak locations of the von Mises stress  $\langle \sigma(\gamma) \rangle$  (Fig. 7 (b)), which indicates that as the strain increases above yielding, the basin geometries change dramatically.

In Fig. 11 (c), we show a scatter plot of  $D$  versus  $W$  for all of the continuous parabolic segments in  $U(\gamma)$  in the range  $0 < \gamma < 0.12$ . We find that more slowly cooled glasses sample basins with larger depths and half-widths,  $D$  and  $W$ , as shown in the upper left inset to panel (c). At small strains, and for all cooling rates, the half-width of the basins scales quadratically with the depth,  $W \sim D^2$  [39]. In contrast,  $W \sim D^\lambda$  with  $\lambda \sim 1.5$  at large strains near and above yielding, which signifies that the dynamics has transitioned from intra-metabasin to inter-metabasin sampling [8, 62]. (See the lower right inset to panel (c).) Recent studies of un-sheared, finite-temperature glasses have also shown that the basin widths and depths are larger for more slowly cooled glasses. However, these studies also showed that the basin curvature is independent of cooling rate, which differs from the results presented in Fig. 10 (a) for glasses undergoing AQS pure shear. Thus, thermal fluctuating systems and glasses undergoing AQS pure shear sample basins with different geometric properties. In summary, we have shown that the geometric properties of basins in the potential energy landscape vary strongly near yielding and depend strongly on cooling rate for glasses undergoing AQS pure shear.

### 3.3. Yielding transition

In this section, we analyze the system-size dependence of the stress and energy losses from rearrangements and softening. Prior studies have shown that quantities, such as the average energy drop and participation number during rearrangements, scale sublinearly with system size in glasses undergoing AQS shear [12, 63]. Other work has shown that changes in the scaling of the rearrangement statistics with system size are associated with the yielding transition [13, 17].

First, note that macroscale quantities, such as the ensemble-averaged stress  $\sigma(\gamma)$  and potential energy per particle  $U(\gamma)$ , are largely independent of system size for  $N \gtrsim 500$ , as shown in Fig. 12. (We discuss the correlation between fluctuations in the local structural quan-

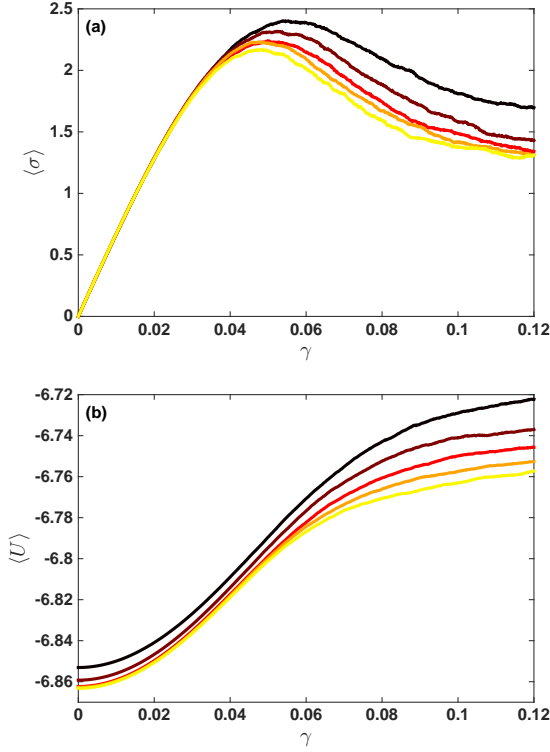


Figure 12: The ensemble-averaged (a) von Mises stress  $\langle \sigma \rangle$  and (b) potential energy per particle  $\langle U \rangle$  versus strain  $\gamma$  for systems prepared at cooling rate  $R = 10^{-5}$  and several system sizes:  $N = 250$  (black), 500 (brown), 1000 (red), 2000 (orange), and 4000 (yellow).  $\langle \sigma \rangle$  and  $\langle U \rangle$  were averaged over at least 500 independent samples.

ties, such as the density and composition, and particle rearrangements in Appendix A.) In Fig 13, we show the system-size dependence of the rearrangement-induced stress loss per strain  $\langle d\sigma_{\text{loss}}^r(\gamma)/d\gamma \rangle$  and energy loss per strain  $\langle dU_{\text{loss}}^r(\gamma)/d\gamma \rangle$ . For  $N \gtrsim 1000$ ,  $\langle d\sigma_{\text{loss}}^r(\gamma)/d\gamma \rangle$  and  $\langle dU_{\text{loss}}^r(\gamma)/d\gamma \rangle$  are nearly independent of system size at small and large strains. However, at strains near the yield strain  $\gamma_y \sim 0.055$ , both  $\langle d\sigma_{\text{loss}}^r(\gamma)/d\gamma \rangle$  and  $\langle dU_{\text{loss}}^r(\gamma)/d\gamma \rangle$  display sharper increases with strain as  $N$  increases. For slowly cooled glasses,  $\langle d\sigma_{\text{loss}}^r(\gamma)/d\gamma \rangle$  forms a peak near yielding (*cf.* Fig. 5 (c)), which persists as the system size increases. In contrast,  $\langle dU_{\text{loss}}^r(\gamma)/d\gamma \rangle$  does not possess a peak and instead displays a sigmoidal form for all cooling rates [25]. The slope of  $\langle dU_{\text{loss}}^r(\gamma)/d\gamma \rangle$  near the midpoint of the sigmoid sharpens with increasing  $N$ , but appears to reach a (cooling-rate dependent) finite value in large systems. The slope of  $\langle dU_{\text{loss}}^r/d\gamma \rangle$  (near the midpoint) for large systems grows with decreasing cooling rate. (See Fig. 16 (a).) The rapid increase in the slope of  $\langle dU_{\text{loss}}^r/d\gamma \rangle$  signals a significant acceleration of rearrangements and energy loss near the yielding transition.

As described in Sec. 3.1 for  $\sigma_{\text{loss}}^r$ , we can also decompose  $dU_{\text{loss}}^r(\gamma)/d\gamma$  into two contributions that give the size  $dU_{\text{loss}}^r(\gamma)/dN_r$  and frequency  $dN_r/d\gamma$  of rearrangements. In Fig. 14, we show the system size dependence

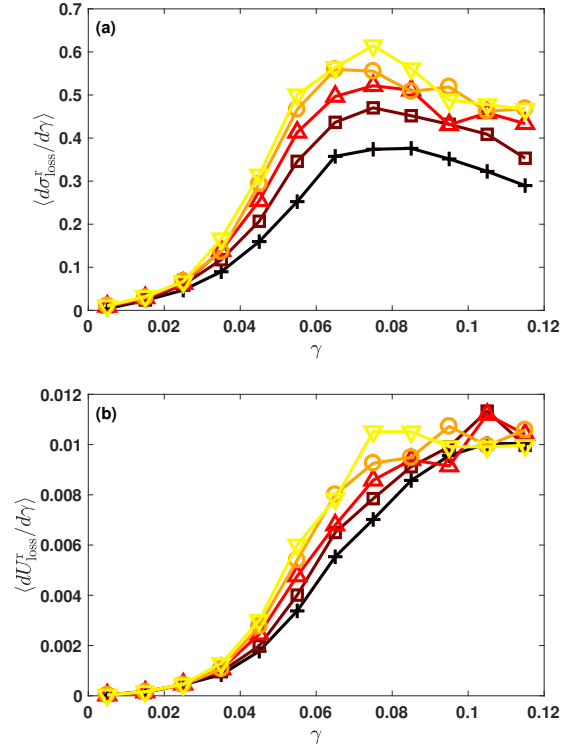


Figure 13: The ensemble-averaged (a) rearrangement-induced stress loss per (1%) strain  $\langle d\sigma_{\text{loss}}^r/d\gamma \rangle$  and (b) rearrangement-induced energy loss per (1%) strain  $\langle dU_{\text{loss}}^r/d\gamma \rangle$  plotted versus strain  $\gamma$  for glasses prepared at cooling rate  $R = 10^{-5}$  and several system sizes:  $N = 250$  (crosses), 500 (squares), 1000 (upward triangles), 2000 (circles), and 4000 (downward triangles). All data points are obtained by averaging over at least 500 independent samples.

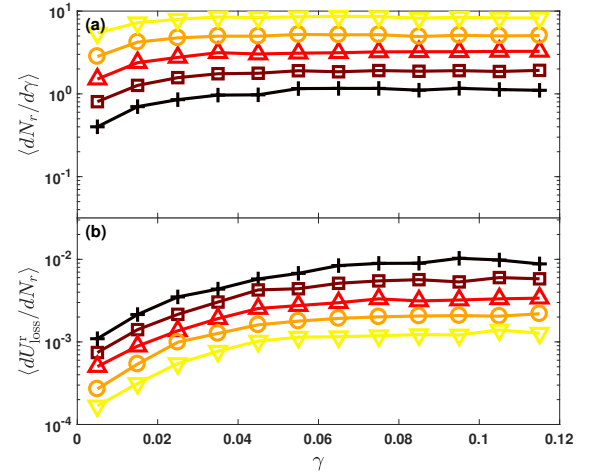


Figure 14: The ensemble-averaged (a) rearrangement frequency  $\langle dN_r/d\gamma \rangle$  and (b) energy loss per rearrangement  $\langle dU_{\text{loss}}^r/dN_r \rangle$  plotted versus strain  $\gamma$  for glasses prepared with cooling rate  $R = 10^{-2}$  and several system sizes:  $N = 250$  (crosses), 500 (squares), 1000 (upward triangles), 2000 (circles), and 4000 (downward triangles). All data points are obtained by averaging over at least 500 samples.

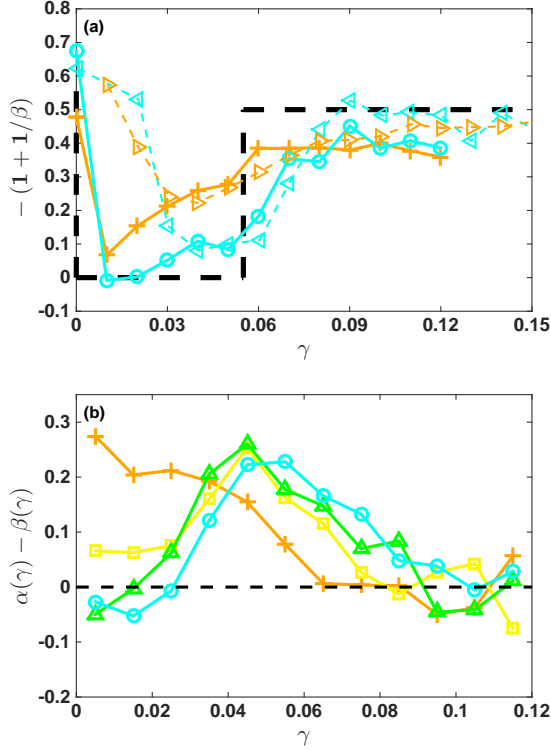


Figure 15: (a) The quantity  $-(1 + 1/\beta(\gamma))$  plotted as a function of strain  $\gamma$  and two cooling rates,  $R = 10^{-2}$  (crosses) and  $10^{-5}$  (circles), where the rearrangement frequency  $\langle dN_r/d\gamma \rangle$  scales as a power law with system size with exponent  $\beta$ :  $\langle dN_r/d\gamma \rangle \sim N^{-\beta}$ . We also show data for  $-(1 + 1/\beta)$  from Hentschel, *et al.* [13] (dashed curves) with “infinitely fast” (rightward triangles) and slow  $R = 10^{-5}$  (leftward triangles) cooling rates. The theoretical prediction for  $-(1 + 1/\beta)$  from Hentschel, *et al.* [13], which is indicated by the black dashed line, has an abrupt increase at the yielding transition. (b) The difference between the scaling exponents  $\alpha(\gamma) - \beta(\gamma)$  is plotted as a function of strain  $\gamma$  for cooling rates  $R = 10^{-2}$  (crosses),  $10^{-3}$  (squares),  $10^{-4}$  (triangles), and  $10^{-5}$  (circles).  $\alpha(\gamma)$  is the system-size scaling exponent for the energy loss per rearrangement:  $\langle dU_{\text{loss}}^r/dN_r \rangle \sim N^{\alpha(\gamma)}$ .

of the ensemble average of these two quantities. As  $N$  increases, the rearrangement size decreases and the frequency increases. Previous studies [12, 13, 53] have focused on the system-size scaling of similar quantities: 1) the strain interval  $\Delta\gamma \sim (dN_r/d\gamma)^{-1}$  between rearrangements and 2) the total energy loss per rearrangement  $\Delta\mathcal{U} \sim NdU_{\text{loss}}^r/dN_r$ .

The ensemble-averaged size and frequency of rearrangements display power-law scaling with system size:

$$\langle dU_{\text{loss}}^r/dN_r \rangle \sim N^{\alpha(\gamma)} \quad (14)$$

$$\langle dN_r/d\gamma \rangle \sim N^{-\beta(\gamma)}, \quad (15)$$

where the scaling exponents  $\alpha(\gamma)$  and  $\beta(\gamma)$  are functions of strain  $\gamma$  and cooling rate  $R$ . In Fig 15 (a), we compare

our results for  $-(1 + 1/\beta(\gamma))$  with those from Ref. [13] for several cooling rates. Ref. [13] provided theoretical arguments for the strain dependence of  $-(1 + 1/\beta(\gamma))$ . They argued that  $-(1 + 1/\beta(\gamma))$  should jump from a nonzero, non-universal value ( $\approx 0.6$  for binary Lennard-Jones glasses) at  $\gamma = 0$  to 0 when  $\gamma > 0$ , then jump discontinuously from zero to a nonzero value at the yield strain  $\gamma_y$ , and remain at a universal value 0.5 as the strain increases beyond  $\gamma_y$ . As shown in Fig 15 (a), our data is qualitatively similar to the data for Ref. [13]. In particular,  $-(1 + 1/\beta(\gamma))$  decreases from a maximal value at  $\gamma = 0$ , remains roughly constant and small over a narrow strain interval below the yield strain, and then begins to increase beyond the yield strain, approaching a plateau value near 0.5 at large strains.

The data in Fig. 15 (a) suggests that  $-(1 + 1/\beta)$  decreases with decreasing cooling rate in the range  $0.04 < \gamma < 0.07$ , but it does not depend strongly on the cooling rate at large strains. Much larger ensemble averages should be performed to confirm these results. Using Eqs. 14 and 15, the rearrangement-induced energy loss per strain obeys  $\langle dU_{\text{loss}}^r/d\gamma \rangle \sim N^{\alpha(\gamma) - \beta(\gamma)}$ . In Fig. 15 (b), we show that the difference in the scaling exponents  $\alpha(\gamma) - \beta(\gamma) \sim 0$  at small and large strains, while  $\alpha(\gamma) - \beta(\gamma) > 0$  near the yield strain. A positive value for  $\alpha(\gamma) - \beta(\gamma)$  indicates that  $\langle dU_{\text{loss}}^r/d\gamma \rangle$  can serve as an order parameter for the yielding transition. The data for  $\alpha(\gamma) - \beta(\gamma)$  for rapidly cooled glasses with  $R = 10^{-2}$  differs from that for more slowly cooled glasses. The stress  $\langle \sigma(\gamma) \rangle$  and stress loss from rearrangements  $\langle d\sigma_{\text{loss}}^r/d\gamma \rangle$  do not possess peaks for rapidly cooled glasses and, in this case, the yield transition behaves as a smooth crossover [13].

In Fig. 16 (b), we plot several characteristic strains (inflection points in  $\langle U(\gamma) \rangle$ ) (Fig. 8 (b)) and  $\langle dU_{\text{loss}}^r/d\gamma \rangle$  (Fig. 16 (a)) and the peak locations of the half-width  $\langle W \rangle$  and depth  $\langle D \rangle$  (Fig. 11 (a) and (b)) of the basins in the PEL), which are correlated with the yielding transition, as a function of cooling rate. At low cooling rates, these measures approach  $\gamma^* \approx 0.055$ . As the cooling rate increases, these characteristic strains decrease. In particular, the measures of the inflection points tend to zero near  $R_c \approx 10^{-1}$ . Note that  $\langle W \rangle$  and  $\langle D \rangle$  do not possess peaks for cooling rates  $R > 10^{-3}$ , and thus these data points are not plotted.

The above results for the rearrangement-induced energy drops were obtained by ensemble averaging over many independent samples at each strain and cooling rate. We will now consider the distribution of energy drops as a function of strain and cooling rate. There have been a number of prior studies of the distribution of rearrangements, spanning length scales from avalanches in earthquakes and other geophysical flows [64, 65], particle rearrangements in driven granular matter [66], serrated flows in bulk metallic glasses [67], and thermally activated particle rearrangements in amorphous alloys [40]. The distribution of energy drops can display power-law scaling or exponential decay depending on the tem-

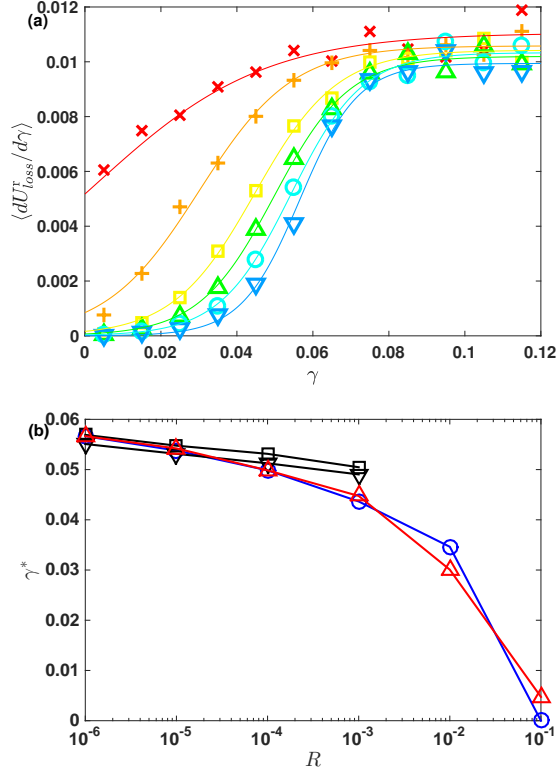


Figure 16: (a) The ensemble-averaged rearrangement-induced energy loss per (1%) strain  $\langle dU_{\text{loss}}^r/d\gamma \rangle$  plotted versus strain  $\gamma$  for glasses with  $N = 2000$  and prepared at several cooling rates:  $R = 10^{-1}$  (crosses),  $10^{-2}$  (plus signs),  $10^{-3}$  (squares),  $10^{-4}$  (upward triangles),  $10^{-5}$  (circles), and  $10^{-6}$  (downward triangles).  $\langle dU_{\text{loss}}^r/d\gamma \rangle$  is obtained by averaging over 500 independent samples. The solid curves are the best-fit logistic functions for each  $R$ . (b) Several characteristic strains  $\gamma^*$  plotted versus cooling rate  $R$  for glasses with  $N = 2000$ . We plot the inflection points for the potential energy  $\langle U(\gamma) \rangle$  (circles) multiplied by  $\approx 1.3$  and potential energy loss per strain  $\langle dU_{\text{loss}}^r/d\gamma \rangle$  (upward triangles) and the location of the peaks in the half-width  $\langle W \rangle$  (squares) and depth  $\langle D \rangle$  (downward triangles) of basins in the potential energy landscape for small  $R$ .

perature and whether the driving is inertial or overdamped [40, 68–70]. For amorphous systems with AQS driving, the form of the distribution of energy drops is typically exponential [43, 53, 63].

In contrast to prior studies, we will characterize the form of the probability distribution  $P(\Delta U)$  of energy drops  $\Delta U$  for each rearrangement both before and after the yielding transition. In Fig. 17, we show  $P(\Delta U)$  from rearrangements before yielding ( $\gamma < 0.055$  in panel (a)) and after yielding ( $\gamma > 0.055$  in panel (b)). Both before and after yielding, the probability distribution decays exponentially:

$$P(\Delta U) = \frac{1}{\kappa} \exp(-\kappa \Delta U), \quad (16)$$

where  $\kappa$  is a function of both strain  $\gamma$  and cooling rate

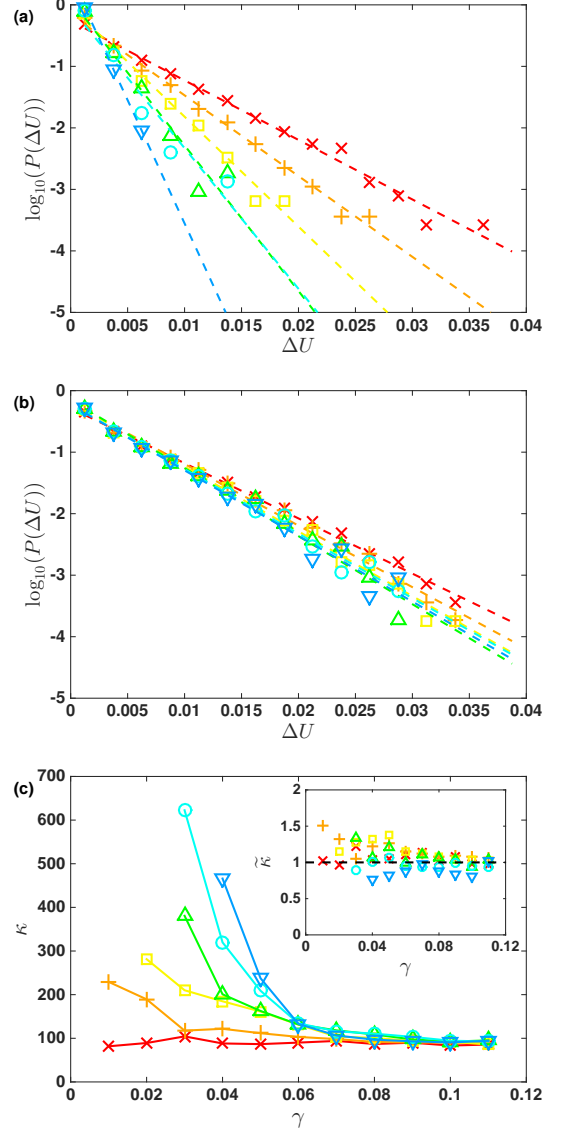


Figure 17: The probability distribution  $P(\Delta U)$  of energy drops (a) before ( $\gamma < 0.055$ ) and (b) after yielding ( $0.055 < \gamma < 0.12$ ) for glasses with  $N = 2000$  and prepared at cooling rates  $R = 10^{-1}$  (crosses),  $10^{-2}$  (plus signs),  $10^{-3}$  (squares),  $10^{-4}$  (upward triangles),  $10^{-5}$  (circles), and  $10^{-6}$  (downward triangles). The distributions have been normalized such that  $\int P(\Delta U)d\Delta U = 1$ . The distributions decay exponentially  $P(\Delta U) \sim \exp(-\kappa\Delta U)$  for all  $R$  above and below the yielding transition. The dashed lines give least-square linear fits for each  $R$ . (c) The coefficient  $\kappa$  of the exponential decay of  $P(\Delta U)$  versus strain for the same cooling rates in (a) and (b). The inset shows the scaled coefficient  $\tilde{\kappa}$  of the exponential decay versus  $\gamma$ .

$R$ . Before the yielding transition,  $\kappa$  depends strongly on cooling rate, *i.e.*  $\kappa$  increases as the cooling rate decreases. Slowly cooled glasses have a relatively low probability for rearrangements with large  $\Delta U$  before yielding. After yielding, the distribution of energy drops is only weakly dependent on cooling rate. In Fig. 17 (c), we plot the

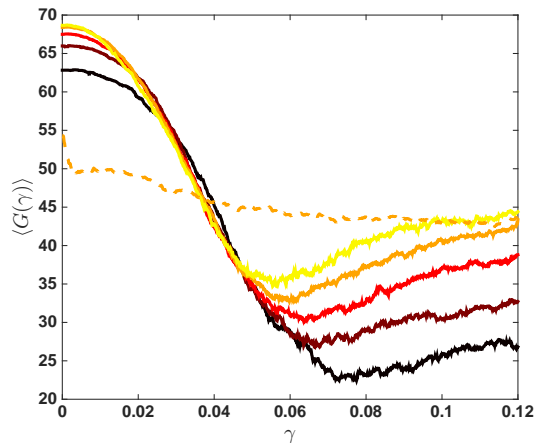


Figure 18: The ensemble-averaged local slope of the continuous stress versus strain segments  $\langle G(\gamma) \rangle$  plotted versus strain  $\gamma$  for glasses prepared with cooling rate  $R = 10^{-5}$  (solid curves) and several system sizes:  $N = 250$  (black), 500 (brown), 1000 (red), 2000 (orange solid curve), and 4000 (yellow).  $\langle G(\gamma) \rangle$  for rapidly cooled glasses with  $R = 10^{-1}$  and  $N = 2000$  is shown for comparison (dashed curve). All data have been averaged over at least 500 samples.

coefficient  $\kappa$  of the exponential decay of the energy drop distribution  $P(\Delta U)$  as a function of strain  $\gamma$  for several cooling rates  $R$ . For more slowly cooled glasses, there is a more rapid decrease in  $\kappa$  before yielding. After yielding,  $\kappa \simeq 100$  is independent of  $\gamma$  and  $R$  and similar to values found in related studies of rearrangements in sheared binary Lennard-Jones glasses [43, 53]. The behavior of the energy scale  $1/\kappa$  mirrors the behavior of the average potential energy  $\langle U(\gamma) \rangle$  (Fig. 8 (b)). We find that  $\tilde{\kappa} = \kappa(a\langle U(\gamma) \rangle + u) \sim 1$ , where  $a \approx 0.1$  is a constant, and  $u/\langle U \rangle \ll 1$  and does not depend on  $\gamma$  or  $R$ . In the inset to Fig. 17 (c), we show  $\tilde{\kappa}$  as a function of  $\gamma$  and  $R$ .

We also studied the system-size dependence of the softening-induced stress and energy losses. The softening-induced stress loss per strain  $\langle d\sigma_{\text{loss}}^s(\gamma)/d\gamma \rangle$  is caused by decreases in the local slopes of the continuous stress versus strain segments. (See Fig. 6.) As the system size increases, the frequency of rearrangements increases (as shown in Fig. 14 (a)) and the lengths of the continuous stress versus strain segments shorten. Here, we investigate whether the local slopes of the continuous stress versus strain segments change significantly with system size.

In Fig. 18, we show  $\langle G(\gamma) \rangle$  for a slowly cooled glass ( $R = 10^{-5}$ ) as a function of system size from  $N = 250$  to 4000.  $\langle G(\gamma) \rangle$  is nearly independent of system size at strains prior to yielding  $\gamma \lesssim 0.055$ . In contrast, at large strains above yielding,  $\langle G(\gamma) \rangle$  grows (and  $\langle d\sigma_{\text{loss}}^s/d\gamma \rangle$  decreases) with  $N$ . We see that for the larger system sizes ( $N > 1000$ )  $\langle G(\gamma) \rangle$  begins to saturate. For comparison, we show  $\langle G(\gamma) \rangle$  for a glass prepared at the highest cooling rate studied,  $R = 10^{-1}$ . At these cooling rates,  $\langle \sigma(\gamma) \rangle$  reaches a large-strain plateau value that is only

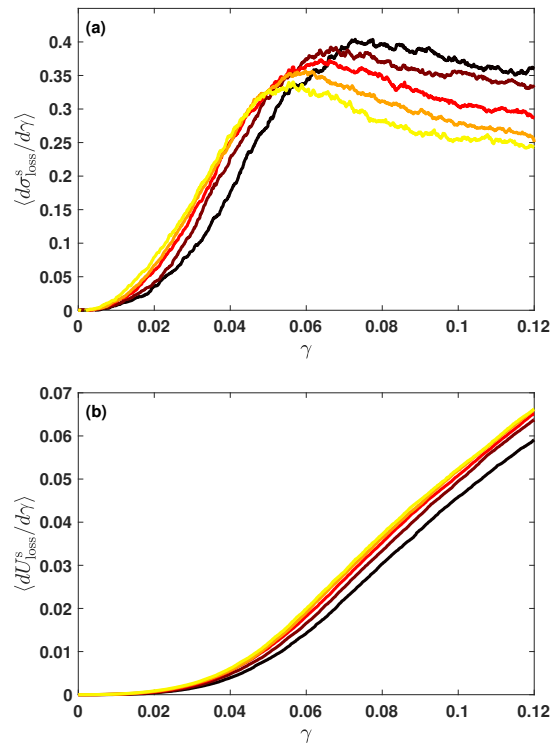


Figure 19: The ensemble-averaged softening-induced (a) stress loss per (1%) strain  $\langle d\sigma_{\text{loss}}^s/d\gamma \rangle$  and (b) energy loss per (1%) strain  $\langle dU_{\text{loss}}^s/d\gamma \rangle$  for a slow cooling rate  $R = 10^{-5}$  and several system sizes:  $N = 250$  (black), 500 (brown), 1000 (red), 2000 (orange), and 4000 (yellow).  $\langle d\sigma_{\text{loss}}^s/d\gamma \rangle$  and  $\langle dU_{\text{loss}}^s/d\gamma \rangle$  were averaged over at least 500 independent samples.

weakly system-size dependent. In Fig. 19, we show the system-size dependence of the softening-induced stress  $\langle d\sigma_{\text{loss}}^s(\gamma)/d\gamma \rangle$  and energy  $\langle dU_{\text{loss}}^s(\gamma)/d\gamma \rangle$  loss per strain. Both quantities saturate for large systems, with forms that are qualitatively the same as those for smaller system sizes. Thus, softening-induced losses appear to persist in the large-system limit.

In this section, we presented results for the system-size dependence of the rearrangement- and softening-induced stress and energy losses from AQS pure shear as a function of strain and cooling rate. Several quantities (both rearrangement- and softening-induced losses) show strong system-size dependence near yielding, which serves to identify the onset of the transition from a solid-like to a flowing state. For example, the potential energy loss per strain  $\langle dU_{\text{loss}}^r/d\gamma \rangle$  from rearrangements shows a sigmoidal form that becomes increasingly sharp in the large systems and the stress loss per strain  $\langle d\sigma_{\text{loss}}^s/d\gamma \rangle$  from softening shows significant system size dependence above yielding, but not below.

#### IV. CONCLUSIONS AND FUTURE DIRECTIONS

In this article, we characterized the nonlinear mechanical response of binary Lennard-Jones glasses subjected to AQS pure shear. We performed comprehensive numerical simulations as a function of strain  $\gamma$  above and below the yielding transition, cooling rates  $R$  used to prepare the zero-temperature glasses over five orders of magnitude, and system sizes ranging from  $N = 250$  to 4000.

To investigate the mechanical response, we focused on global quantities, such as the von Mises stress  $\sigma$  and total potential energy per particle  $U$ . Though it is hidden when taking an ensemble average,  $\sigma(\gamma)$  and  $U(\gamma)$  for each single glass configuration are composed of continuous segments in strain punctuated by rapid drops in either stress or energy caused by particle rearrangements. Thus, deviations (losses for the cooling rates considered here) in the stress or potential energy from elastic behavior originate from two sources: 1) softening-induced losses from changes in the form of the continuous segments in strain and 2) rearrangement-induced losses that depend on the frequency and size of the energy or stress drops. A key feature of this study is that we decomposed the total stress and energy losses into contributions from both sources.

In general, both softening- and rearrangement-induced losses are small well below the yield strain, and then they begin to increase rapidly near yielding. Near and above yielding, both types of losses contribute to the nonlinear mechanical response and remain finite as the system size increases. In the range of cooling rates studied here, rearrangement-induced stress losses are larger than softening-induced stress losses. However, the softening-induced stress losses increase with decreasing cooling rate (Fig. 7 (a)), and thus softening-induced stress losses can dominate the nonlinear mechanical response at sufficiently small cooling rates.

In many cases, the yield strain, where sheared glasses transition from a disordered solid into a flowing state, is difficult to pinpoint because many physical quantities, such as the shear stress and potential energy, vary smoothly with strain [55]. Here, we identified several quantities that show significant changes as the strain is increased above yielding. First, geometric features (*i.e.* the half-width  $W$  and depth  $D$ ) of basins in the PEL along the strain direction develop peaks near the yield strain for slowly cooled glasses. In addition, the scaling relation between the half-width and depth  $D \sim W^\lambda$  changes from a scaling exponent of  $\lambda = 2$  below yielding to 1.5 above yielding for all cooling rates studied. Second, the rearrangement-induced energy loss per strain  $\langle dU_{\text{loss}}^r/d\gamma \rangle$  possesses a sigmoidal form with a slope near the yield strain that becomes sharper as the cooling rate decreases and system size increases. Further, we decomposed the rearrangement-induced energy loss per strain  $\langle dU_{\text{loss}}^r/d\gamma \rangle$  into two terms that determine the size and frequency of rearrangements, and showed

that the system-size scaling of these two terms changes near the yielding transition [13]. Third, as found previously, the distribution of energy drops decays exponentially for AQS sheared glasses over the full range of strain [43, 53, 63]. However, the energy scale of the exponential decay depends strongly on the cooling rate below yielding, while it is cooling-rate independent above yielding.

In future studies, we will investigate several new directions related to the mechanical properties of glasses. In this article, we focused on glasses that were prepared by cooling them to zero temperature at different rates. However, glasses can also be prepared by cooling them to a nonzero value  $T_A$  below the glass transition temperature and aging the system (*i.e.* maintaining a fixed  $T_A$  for a given amount of time  $t_A$ ). Both  $T_A$  and  $t_A$  can affect the mechanical properties of BMGs. Previous studies have found that when the aging temperature is near but below the glass transition temperature,  $T_A \lesssim T_g$ , the free volume of the system decreases and glasses can become brittle [26, 71, 72]. In addition, the impact toughness decreases with increasing aging time and temperature [73]. In our future computational studies, we will disentangle the separate effects of particle rearrangements and softening on the mechanical response of glasses for different aging protocols.

Second, the current computational studies were performed using AQS pure shear [43]. How will the results we presented change when we consider glasses sheared at finite shear rate  $\dot{\gamma}$  and temperature  $T$ ? Suppose the timescale for structural relaxation from thermal fluctuations is given by  $\tau$ . In the case  $\dot{\gamma}\tau \ll 1$ , we expect similar results to those presented here. As the temperature increases, the system will sample higher regions of the PEL than sampled at zero temperature. The frequency of particle rearrangements will increase for  $T > 0$  as rearrangements become thermally activated instead of strain-induced mechanical instabilities [74, 75]. In future studies, we will analyze the rearrangement- and softening-induced losses at finite temperature and strain rate to determine their effects on the stress versus strain curve [52, 76], yield strain [8], and ductility [77].

The computational studies presented here were also performed using strain control. In contrast, many experiments probe the mechanical response of glasses by performing creep studies at fixed applied shear stress [67–69]. For computational studies at fixed shear stress, the system will flow until it finds a glass configuration with a shear stress that matches the applied shear stress [78, 79]. If the system cannot find a configuration that can balance the applied shear stress, the system will flow indefinitely with a well-defined average shear rate. In future studies, we will compare the rearrangement- and softening-induced stress and energy losses in the fixed shear stress, fixed strain, and fixed strain-rate ensembles.

In previous computational studies, we showed that sheared frictionless granular materials, which interact via purely repulsive interactions, possess monotonic stress

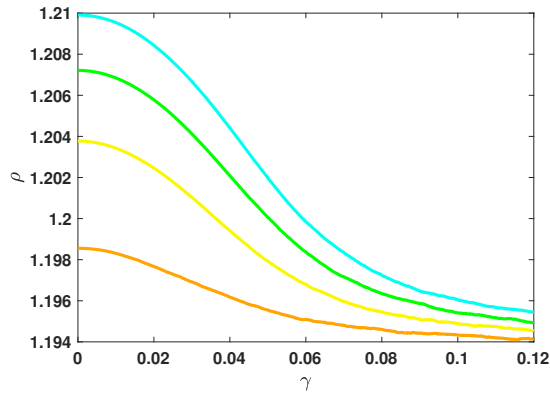


Figure 20: Reduced number density  $\rho = N\sigma_{AA}^3/V$  of binary Lennard-Jones glasses containing  $N = 2000$  particles prepared using cooling rates  $R = 10^{-2}$  (orange),  $R = 10^{-3}$  (yellow),  $R = 10^{-4}$  (green) and  $R = 10^{-5}$  (cyan). These systems undergo AQS pure shear at constant pressure  $P = 10^{-8}$  as a function of strain  $\gamma$ . Each curve is averaged over 500 independent samples.

versus strain curves even for “slowly cooled” granular samples [80]. Based on our current results for rapidly cooled binary Lennard-Jones glasses, we expect that the stress and potential energy losses in frictionless granular materials are dominated by rearrangement-induced losses. In future studies, we will determine the relative contributions of rearrangement- and softening-induced stress and energy losses as a function of the strength and range of the attractive interactions in the interatomic potential. In particular, recent studies [81, 82] have shown that the form of the interaction potential can influence the ductility of amorphous alloys, and thus we will investigate the relative contributions of rearrangement- and softening-induced losses in ductile versus brittle glasses.

### Acknowledgments

The authors acknowledge primary financial support from NSF MRSEC DMR-1119826 (K.Z.) and partial support from NSF Grant Nos. CMMI-1462439 (C.O. and M.F.) and CMMI-1463455 (M.S.). This work was supported by the High Performance Computing facilities operated by, and the staff of, the Yale Center for Research Computing.

### Appendix A: Fluctuations in local density, composition, and particle contacts from rearrangements

In the main text, we focused on the global mechanical response ( $\langle\sigma(\gamma)\rangle$  and  $\langle U(\gamma)\rangle$ ) of zero-temperature binary Lennard-Jones glasses to AQS shear. There have been several prior studies that have attempted to connect par-

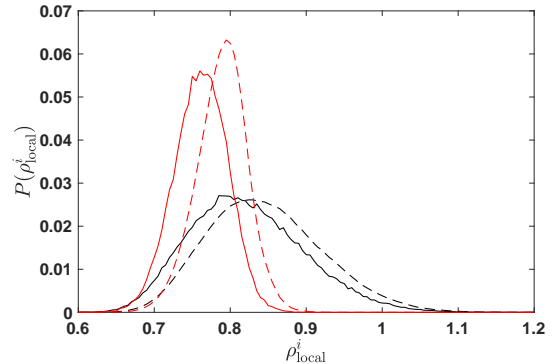


Figure 21: The probability distribution of local density  $P(\rho_{\text{local}}^i)$  for each particle  $i$  of large particles (black curves) and small particles (red curves), which are either mobile (solid curves) or non-mobile (dashed curves) during rearrangements, in binary Lennard-Jones glasses prepared using cooling rate  $R = 10^{-6}$  undergoing AQS pure shear from strain  $\gamma = 0$  to 0.12. Data for  $P(\rho_{\text{local}}^i)$  is collected before each rearrangement event and includes 10,336 rearrangements in 200 independent samples.

ticle rearrangements during shear to local properties of the glass. For example, studies have shown that more loosely packed glasses with reduced short- to medium-range structural order are more prone to particle rearrangements and energy loss during shear [83]. Other studies have identified shear transformation zones by correlating soft modes from the density of vibrational modes with regions of the system with low local yield stress or elevated free volume [48, 50]. In this Appendix, we relate our work to these prior studies by quantifying the fluctuations in local structural quantities (such as the density, composition, and interparticle contacts) following shear-induced rearrangements.

Since the systems are sheared at fixed pressure, the global number density  $\rho$  varies with strain. In Fig. 20, we plot the density as a function of pure shear strain for several cooling rates. At zero strain, the density is smaller for more rapidly cooled glasses (with more free volume). Furthermore, as strain increases, the density decreases for systems prepared at all cooling rates considered, since more free volume is generated during shear. The overall decrease in density is smaller for the more rapidly cooled glasses since they are already loosely packed at zero strain. We also find that the Poisson’s ratio  $\nu$  increases with cooling rate (indicating enhanced ductility at higher cooling rates), but remains  $0 < \nu < 0.5$  [25].

We identify mobile and non-mobile particles in each rearrangement event by calculating the participation number  $\mathcal{P}$  [41]. We identify the  $\mathcal{P}$  particles with largest displacements as the mobile particles and the other  $N - \mathcal{P}$  particles as the non-mobile particles. We quantify the local properties of the system (i.e., density, composition, and interparticle contacts) of mobile and non-mobile particles at strain  $\gamma_r - \delta\gamma$  immediately before a rearrangement event at  $\gamma_r$ . We perform Voronoi tessellation at

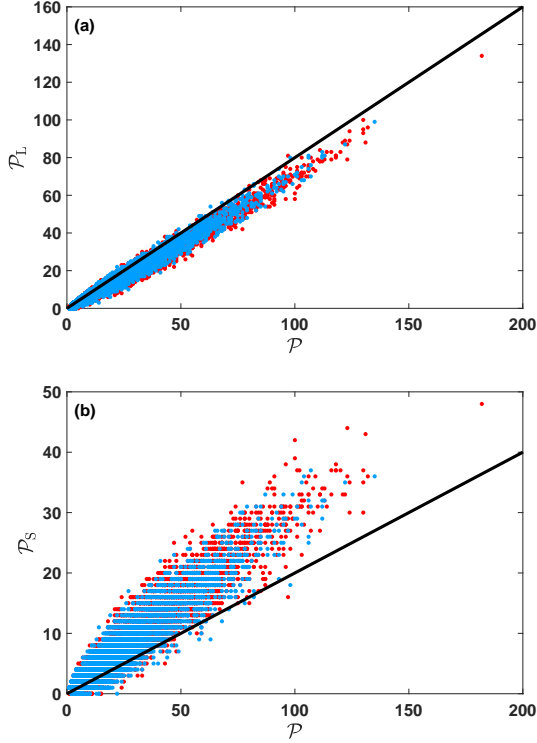


Figure 22: The number of (a) large particles  $\mathcal{P}_L$  and (b) small particles  $\mathcal{P}_S$  plotted versus the participation number  $\mathcal{P}$ . Each dot represents a single rearrangement event in 200 independent binary Lennard-Jones glasses prepared using cooling rate  $R = 10^{-6}$  (blue dots) and  $R = 10^{-1}$  (red dots) undergoing AQS pure shear from strain  $\gamma = 0$  to 0.12. The solid lines have slopes 0.8 and 0.2 in (a) and (b), respectively, which represent the homogenous particle compositions.

strain  $\gamma_r - \delta\gamma$  to determine the local particle density and the neighbors of each particle before the rearrangement. We define the normalized local density for particle  $i$  as  $\rho_{\text{local}}^i = \pi r^3 / 6V_{\text{local}}^i$ , where  $r$  is the interparticle separation at which the force on given particle and its neighbors is zero and  $V_{\text{local}}^i$  is the volume of the Voronoi cell for particle  $i$ . The probability distribution  $P(\rho_{\text{local}}^i)$  over a range of pure shear strain  $\gamma = 0$  to 0.12 is shown in Fig. 21. We find that the peak in  $P(\rho_{\text{local}}^i)$  for mobile particles is smaller than that for non-mobile particles, for both large and small particles. These results are consistent with prior studies that state that shear transformation zones possess excess free volume and are more loosely packed.

We also quantified the composition of large and small particles in the mobile and non-mobile regions of the system for each rearrangement. In Fig. 22, we show that the proportion of large mobile particles is less than the homogeneous value (80%), while the proportion of small mobile particles is more than the homogeneous value (20%). Thus, small particles are more likely than large particles to participate in particle rearrangements.

In addition, we measured the fractions of interparticle contacts (large-large (LL), large-small (LS), and small-

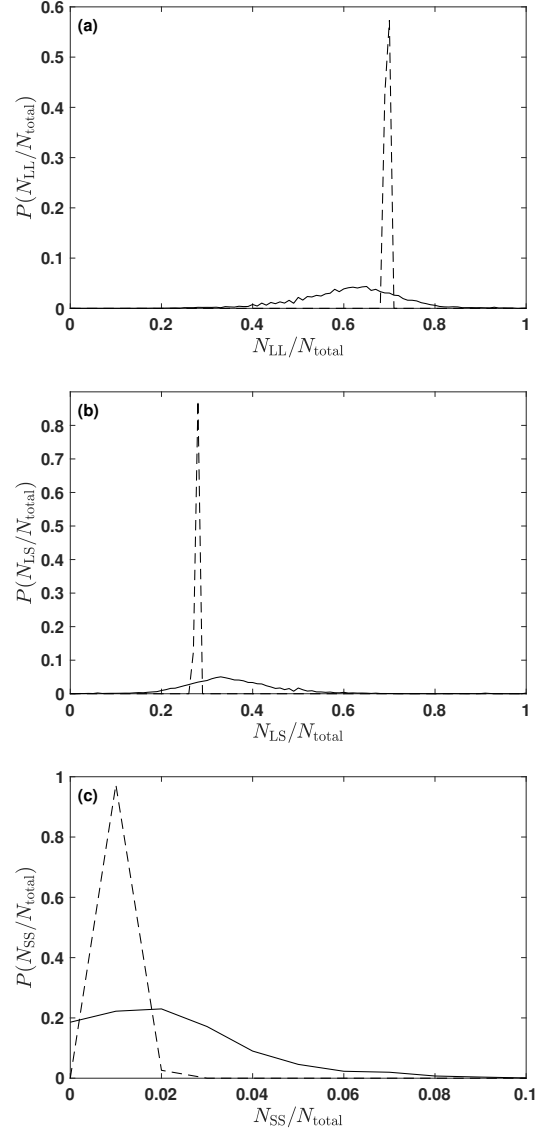


Figure 23: Distribution of the fractions of (a) large-large  $N_{LL}/N_{\text{total}}$ , (b) large-small  $N_{LS}/N_{\text{total}}$ , and (c) small-small  $N_{SS}/N_{\text{total}}$  contacts for mobile (solid curves) and non-mobile (dashed curves) particles during rearrangements for binary Lennard-Jones glasses prepared using cooling rate  $R = 10^{-6}$  and subjected to athermal, quasistatic pure shear from strain  $\gamma = 0$  to 0.12. Note that  $N_{\text{total}} = N_{LL} + N_{LS} + N_{SS}$ . Data for the fraction of large-large, large-small, and small-small contacts is collected before each of the 10,336 rearrangement events from 200 independent samples.

small (SS)) for mobile and non-mobile particles during rearrangements. In Fig. 23, we show that mobile particles possess more small-small and large-small contacts than non-mobile particles, and less large-large contacts than non-mobile particles. This result is consistent with those shown in Fig. 22 since it shows that there are more small mobile particles and less large mobile particles than the homogeneous values. Our results for the local density

and composition fluctuations are very weakly dependent on the cooling rate used to prepare the glasses and the

total strain.

- 
- [1] M. D. Ediger, C. Angell, and S. R. Nagel, *J. Phys. Chem.* **100**, 13200 (1996).
- [2] L. Berthier and G. Biroli, *Rev. Mod. Phys.* **83**, 587 (2011).
- [3] W. L. Johnson, *MRS bulletin* **24**, 42 (1999).
- [4] A. Inoue and N. Nishiyama, *MRS Bulletin* **32**, 651 (2007).
- [5] M. Kanik, P. Bordeenithikasem, G. Kumar, E. Kinser, and J. Schroers, *Appl. Phys. Lett.* **105**, 131911 (2014).
- [6] M. Kanik, P. Bordeenithikasem, D. Kim, N. Selden, A. Desai, R. MCloskey, and J. Schroers, *Journal of Microelectromechanical Systems* **24**, 19 (2015).
- [7] M. Ashby and A. Greer, *Scripta Mater.* **54**, 321 (2006).
- [8] W. L. Johnson and K. Samwer, *Phys. Rev. Lett.* **95**, 195501 (2005).
- [9] J. Schroers, *Phys. Today* **66**, 32 (2013).
- [10] P. G. Debenedetti and F. H. Stillinger, *Nature* **410**, 259 (2001).
- [11] C. Deng and C. A. Schuh, *Appl. Phys. Lett.* **100**, 251909 (2012).
- [12] S. Karmakar, E. Lerner, and I. Procaccia, *Phys. Rev. E* **82**, 055103 (2010).
- [13] H. G. E. Hentschel, P. K. Jaiswal, I. Procaccia, and S. Sastry, *Phys. Rev. E* **92**, 062302 (2015).
- [14] P. K. Jaiswal, I. Procaccia, C. Rainone, and M. Singh, *Phys. Rev. Lett.* **116**, 085501 (2016).
- [15] D. V. Denisov, M. T. Dang, B. Struth, A. Zaccone, G. H. Wegdam, and P. Schall, *Sci. Rep.* **5**, 14359 (2014).
- [16] T. Kawasaki and L. Berthier, *Phys. Rev. E* **94**, 022615 (2016).
- [17] P. Leishangthem, A. D. Parmar, and S. Sastry, *Nature Commun.* **8** (2017).
- [18] C. C. Hays, C. P. Kim, and W. L. Johnson, *Phys. Rev. Lett.* **84**, 2901 (2000).
- [19] J. Lewandowski, W. Wang, and A. Greer, *Philos. Mag. Lett.* **85**, 77 (2005).
- [20] G. Kumar, S. Prades-Rodel, A. Blatter, and J. Schroers, *Scr. Mater.* **65**, 585 (2011).
- [21] J. Ketkaew, H. Wang, W. Chen, M. Fan, G. Pereira, Z. Liu, W. Dmowski, E. Bouchbinder, M. D. Shattuck, C. S. O'Hern, et al., "Fictive temperature controlling ductility in metallic glasses as a mechanical glass transition", Submitted (2017).
- [22] A. Q. Tool, *Journal of the American Ceramic society* **29**, 240 (1946).
- [23] O. Narayanaswamy, *Journal of the American Ceramic Society* **54**, 491 (1971).
- [24] C. T. Moynihan, A. J. Easteal, M. A. Bolt, and J. Tucker, *J. Am. Ceram. Soc.* **59**, 12 (1976).
- [25] M. Fan, M. Wang, K. Zhang, Y. Liu, J. Schroers, M. D. Shattuck, and C. S. O'Hern, *Phys. Rev. E* **95**, 022611 (2017).
- [26] C. H. Rycroft and E. Bouchbinder, *Phys. Rev. Lett.* **109**, 194301 (2012).
- [27] G. Kumar, P. Neibecker, Y. H. Liu, and J. Schroers, *Nature Commun.* **4**, 1536 (2013).
- [28] W. Li, H. Bei, Y. Tong, W. Dmowski, and Y. Gao, *Appl. Phys. Lett.* **103**, 171910 (2013).
- [29] N. Nollmann, I. Binkowski, V. Schmidt, H. Rösner, and G. Wilde, *Scr. Mater.* **111**, 119 (2016).
- [30] J. Zemp, M. Celino, B. Schönfeld, and J. F. Löffler, *Phys. Rev. Lett.* **115**, 165501 (2015).
- [31] M. Utz, P. G. Debenedetti, and F. H. Stillinger, *Phys. Rev. Lett.* **84**, 1471 (2000).
- [32] A. J., E. Bouchbinder, and I. Procaccia, *Phys. Rev. E* **87**, 042310 (2013).
- [33] F. H. Stillinger, *Science* **267**, 1935 (1995).
- [34] P. Charbonneau, J. Kurchan, G. Parisi, P. Urbani, and F. Zamponi, *Nature Commun.* **5** (2014).
- [35] C. O'Hern, *Physics* **9**, 133 (2016).
- [36] H.-B. Yu, R. Richert, R. Maaß, and K. Samwer, *Nature Commun.* **6** (2015).
- [37] I. Regev, J. Weber, C. Reichhardt, K. A. Dahmen, and T. Lookman, *Nature Commun.* **6**, 8805 (2015).
- [38] D. Fiocco, G. Foffi, and S. Sastry, *Phys. Rev. Lett.* **112**, 025702 (2014).
- [39] Y. Fan, T. Iwashita, and T. Egami, *Nature Commun.* **5**, 5083 (2014).
- [40] Y. Fan, T. Iwashita, and T. Egami, *Phys. Rev. Lett.* **115**, 045501 (2015).
- [41] D. L. Malandro and D. J. Lacks, *J. Chem. Phys.* **110**, 4593 (1999).
- [42] D. J. Lacks and M. J. Osborne, *Phys. Rev. Lett.* **93**, 255501 (2004).
- [43] C. E. Maloney and A. Lemaître, *Phys. Rev. E* **74**, 016118 (2006).
- [44] S. Saw, S. Abraham, and P. Harrowell, *Physical Review E* **94**, 022606 (2016).
- [45] A. Argon and H. Kuo, *Mater. Sci. Eng.* **39**, 101 (1979).
- [46] M. L. Falk and J. S. Langer, *Phys. Rev. E* **57**, 7192 (1998).
- [47] J. S. Langer, *Phys. Rev. E* **77**, 021502 (2008).
- [48] S. Patinet, D. Vandembroucq, and M. L. Falk, *Phys. Rev. Lett.* **117**, 045501 (2016).
- [49] A. Widmer-Cooper, H. Perry, P. Harrowell, and D. R. Reichman, *Nature Phys.* **4**, 711 (2008).
- [50] J. Ding, S. Patinet, M. L. Falk, Y. Cheng, and E. Ma, *Proc. Natl. Acad. Sci.* **111**, 14052 (2014).
- [51] J. S. Harmon, M. D. Demetriou, W. L. Johnson, and K. Samwer, *Phys. Rev. Lett.* **99**, 135502 (2007).
- [52] A. K. Dubey, I. Procaccia, C. A. B. Z. Shor, and M. Singh, *Phys. Rev. Lett.* **116**, 085502 (2016).
- [53] E. Lerner and I. Procaccia, *Phys. Rev. E* **79**, 066109 (2009).
- [54] V. Chikkadi, O. Gendelman, V. Ilyin, J. Ashwin, I. Procaccia, and C. A. Shor, *Europhys. Lett.* **110**, 48001 (2015).
- [55] I. Regev, T. Lookman, and C. Reichhardt, *Phys. Rev. E* **88**, 062401 (2013).
- [56] W. Kob and H. C. Andersen, *Phys. Rev. E* **51**, 4626 (1995).
- [57] M. P. Allen and D. J. Tildesley, *Computer simulation of liquids* (Oxford University Press, 1989).
- [58] S. Plimpton, *J. Comput. Phys.* **117**, 1 (1995).

- [59] M. E. Tuckerman, J. Alexandre, R. López-Rendón, A. L. Jochim, and G. J. Martyna, *J. Phys. A: Math. Gen.* **39**, 5629 (2006).
- [60] J. Wittmer, H. Xu, P. Polińska, F. Weysser, and J. Baschnagel, *The Journal of chemical physics* **138**, 12A533 (2013).
- [61] S. Büchner and A. Heuer, *Phys. Rev. E* **60**, 6507 (1999).
- [62] C. E. Maloney and D. J. Lacks, *Phys. Rev. E* **73**, 061106 (2006).
- [63] C. Maloney and A. Lemaître, *Phys. Rev. Lett.* **93**, 016001 (2004).
- [64] P. Bak and C. Tang, *J. Geophys. Res* **94**, 635 (1989).
- [65] H. Kawamura, T. Hatano, N. Kato, S. Biswas, and B. K. Chakrabarti, *Rev. Mod. Phys.* **84**, 839 (2012).
- [66] D. Denisov, K. Lörincz, J. Uhl, K. Dahmen, and P. Schall, *Nature Commun.* **7** (2016).
- [67] J. Antonaglia, W. J. Wright, X. Gu, R. R. Byer, T. C. Hufnagel, M. LeBlanc, J. T. Uhl, and K. A. Dahmen, *Phys. Rev. Lett.* **112**, 155501 (2014).
- [68] J. Antonaglia, X. Xie, G. Schwarz, M. Wraith, J. Qiao, Y. Zhang, P. K. Liaw, J. T. Uhl, and K. A. Dahmen, *Sci. Rep.* **4**, 4382 (2014).
- [69] B. A. Sun, H. B. Yu, W. Jiao, H. Y. Bai, D. Q. Zhao, and W. H. Wang, *Phys. Rev. Lett.* **105**, 35501 (2010).
- [70] K. M. Salerno, C. E. Maloney, and M. O. Robbins, *Phys. Rev. Lett.* **109**, 105703 (2012).
- [71] P. Murali and U. Ramamurty, *Acta Materialia* **53**, 1467 (2005).
- [72] Q. Luo, B. Zhang, D. Zhao, R. Wang, M. Pan, and W. Wang, *Applied physics letters* **88**, 151915 (2006).
- [73] U. Ramamurty, M. Lee, J. Basu, and Y. Li, *Scripta Materialia* **47**, 107 (2002).
- [74] A. Lemaître and C. Caroli, *Phys. Rev. Lett.* **103**, 065501 (2009).
- [75] S. Karmakar, E. Lerner, I. Procaccia, and J. Zylberg, *Phys. Rev. E* **82**, 031301 (2010).
- [76] J. Rottler and M. O. Robbins, *Phys. Rev. E* **68**, 011507 (2003).
- [77] H. B. Yu, X. Shen, Z. Wang, L. Gu, W. H. Wang, and H. Y. Bai, *Phys. Rev. Lett.* **108**, 015504 (2012).
- [78] V. Dailidonis, V. Ilyin, P. Mishra, and I. Procaccia, *Phys. Rev. E* **90**, 052402 (2014).
- [79] J. Lin, T. Gueudré, A. Rosso, and M. Wyart, *Phys. Rev. Lett.* **115**, 168001 (2015).
- [80] N. Xu and C. S. O'Hern, *Phys. Rev. E* **73**, 061303 (2006).
- [81] Y. Shi, J. Luo, F. Yuan, and L. Huang, *J. Appl. Phys.* **115**, 043528 (2014).
- [82] O. Dauchot, S. Karmakar, I. Procaccia, and J. Zylberg, *Phys. Rev. E* **84**, 046105 (2011).
- [83] K.-W. Park, C.-M. Lee, M. Wakeda, Y. Shibutani, M. L. Falk, and J.-C. Lee, *Acta Materialia* **56**, 5440 (2008).